

Soft Matter

Capillary imbibition of confined monodisperse emulsions in microfluidic channels

Journal:	Soft Matter	
Manuscript ID	SM-ART-02-2024-000179.R1	
Article Type:	Paper	
Date Submitted by the Author:	09-Apr-2024	
Complete List of Authors:	Norouzi Darabad, Masoud; Texas Technical University, Department of Chemical Engineering Singha, Sagnik; Texas Tech University, Mechanical Engineering Vanapalli, Siva; Texas Tech University, Chemical Engineering Vaughn, Mark; Texas Tech University, Chemical Engineering Blawzdziewicz, Jerzy; Texas Tech University, Department of Mechanical Engineering	

SCHOLARONE™ Manuscripts Page 1 of 21 Soft Matter

Journal Name



ARTICLE TYPE

Cite this: DOI: 10.1039/xxxxxxxxxx

Capillary imbibition of confined monodisperse emulsions in microfluidic channels[†]

Masoud Norouzi Darabad, a Sagnik Singha, b‡ Siva A. Vanapalli, a Mark W. Vaughn *a and Jerzy Blawzdziewicz *bc

Received Date Accepted Date

DOI: 10.1039/xxxxxxxxxx

www.rsc.org/journalname

We study imbibition of a monodisperse emulsion into high-aspect ratio microfluidic channels with the height h comparable to the droplet diameter d. Two distinct regimes are identified in the imbibition dynamics. In a strongly confined system (the confinement ratio d/h=1.2 in our experiments), the droplets are flattened between the channel walls and move more slowly compared to the average suspension velocity. As a result, a droplet-free region forms behind the meniscus (separated from the suspension region by a sharp concentration front) and the suspension exhibits strong droplet-density and velocity fluctuations. In a weaker confinement, d/h=0.65, approximately spherical droplets move faster than the average suspension flow, causing development of a dynamically unstable high-concentration region near the meniscus. This instability results in the formation of dense droplet clusters, which migrate downstream relative to the average suspension flow, thus affecting the entire suspension dynamics. We explain the observed phenomena using linear transport equations for the particle-phase and suspension fluxes driven by the local pressure gradient. We also use a dipolar particle interaction model to numerically simulate the imbibition dynamics. The observed large velocity fluctuations in strongly confined systems are elucidated in terms of migration of self-assembled particle chains with highly anisotropic mobility.

1 Introduction

Capillary imbibition is a process in which a fluid driven by interfacial forces is spontaneously absorbed into a pore. The imbibition plays an important role in many natural and man-made systems that involve fluid transport in elongated pores or pore networks. The earliest known account of an investigation of fluid imbibition can be found in Leonardo da Vinci's Hammer Codex, where he presented an imbibition-driven self-priming siphon. ^{1,2} The first modern analysis of the capillary imbibition of Newtonian fluids was performed by Washburn. ³ He demonstrated that in the viscous-dominated regime the square of the fluid penetration length into a capillary is a linear function of the imbibition time. Deviations from Washburn's prediction due to inertial forces ^{4,5}, contact angle ⁶ and capillary number ^{7,8} changes, and variations

in capillary geometry 9-11 were subsequently investigated.

In present-day technological applications imbibition is used for fluid manipulation in lab-on-a-chip and medical-testing devices, ^{12,13} and its control is crucial for optimization of oil recovery from porous rocks ¹⁴ and enhancing the quality of ink-jet printing. ¹⁵ For complex fluids, capillary imbibition has numerous applications in bioengineering, manufacturing of advanced materials, and development of microfluidic platforms. Examples include penetration of blood and other non-Newtonian fluids into microcapillaries, ^{16–18} flow of polymers in nano-porous materials, ¹⁹ and capillary-driven flows used in fabrication of nano-composite materials ²⁰ and in optofluidics. ²¹

In addition to its practical applications, capillary imbibition of complex fluids provides a convenient platform for studying microscale dynamics of dispersed-phase materials. Especially interesting is the behavior of suspension under quasi-2D confinement d/h = O(1), where d is the particle diameter and h is the smallest dimension of the channel. In such systems the relative motion between the continuous and dispersed phases is enhanced, leading to a rich confinement-dependent phenomenology.

While there have been numerous studies of imbibition of single-phase complex fluids, $^{18,22-27}$ there are only a few studies of capillary imbibition of suspensions. Zhou *et al.* 16 and Holloway *et al.* 28 investigated imbibition of blood-cell suspensions 16 and sus-

^{*} Corresponding authors

^a Department of Chemical Engineering, Texas Tech University, Box 43121 Lubbock, TX 79409, USA.

b Department of Mechanical Engineering, Texas Tech University, Box 41021, Lubbock, TX 79409, USA.

^c Department of Physics and Astronomy, Texas Tech University, Box 41051, Lubbock, TX 79409. USA

[†] Electronic Supplementary Information (ESI) available. See DOI 10.1039/b000000x/

[‡] Present address: High Performance Computing Center, Texas Tech University, Box 41167, Lubbock, TX, 79409, USA

Soft Matter Page 2 of 21

pensions of rigid particles ²⁸ into capillaries of a diameter much larger than the particle size. They demonstrated that the particles tend to accumulate next to the meniscus, which modifies Washburn scaling and may lead to capillary clogging. Formation of a disordered dense particle band and its effect on the dynamics of the meniscus were also reported for pressure-driven flows. ^{29,30}

At a stronger confinement, $d/h \gtrsim 1$, the phenomenon of droplet congregation near the air-fluid meniscus was recently used by Abedi, Chen, and Vanapalli to generate 2D closely packed hexagonally ordered droplet arrays in a study of avalanches of drop coalescence events. ^{31,32} However, there does not appear to be available a systematic investigation of suspension imbibition for different d/h = O(1) quasi-2D confinement conditions.

We note that the pressure-driven flow of strongly confined suspensions in the Hele–Shaw geometry has been well studied, ^{33–35} and it was shown that interactions between droplets or particles in Hele–Shaw cells can exhibit fascinating collective behavior. (Examples include density waves in 1D droplet arrays, ³⁶ spontaneous formation of continuous or fragmented chain structures, ³⁷ hydrodynamic stabilization of 2D ordered particle arrays, ^{33,38} dislocations and fingering instabilities in such hydrodynamic crystals, ³³ and Burgers shock-waves. ^{34,39}) The observed complex collective dynamics stem, primarily, from the far-field dipolar Hele-Shaw hydrodynamic interactions between confined particles. ^{36,40,41} The effects of higher-order contributions ^{41–43} on the microscale evolution ^{33,43} and the macroscopic suspension dynamics ⁴⁴ have also been investigated. Similar mechanisms are important in emulsion imbibition.

We study two cases of capillary imbibition of emulsions in thin, high aspect-ratio rectangular microfluidic channels where the droplets form a monolayer. For $d/h \gtrsim 1$, the droplets, which are flattened by the channel walls, have a circular disk-like shape, and for $d/h \lesssim 1$, the droplets remain spherical.

We explain how microscale droplet interactions result in distinct macroscale dynamics in these two cases. For disk-like droplets, a droplet-free zone with a sharp boundary between the droplet-free region and suspension region forms behind the meniscus. (Droplet depletion from the meniscus has also been reported for weakly confined non-neutrally buoyant droplets during suspension imbibition. ⁴⁵) For weaker confinement, spherical droplets form a densely packed accumulation region behind the mensicus that undergoes fingering instability. This affects particle distribution and may cause strong deformation of the meniscus.

To shed light on the experimental observations, we use two coupled linear transport equations to describe suspension flow and particle-phase dynamics. From our experimental data we evaluate the transport coefficients that link the suspension and particle-phase velocities to the local pressure gradient. We show that both coarse-grained transport equations are needed to explain the wealth of phenomena occurring in the imbibition process. In addition to the phenomenological macroscopic description, we carry out a microscopic analysis of particle cluster motion and perform numerical simulations of particle dynamics using a dipolar-interaction model. Experimental measurements are compared with a pressure-driven flow of hard-sphere monolayers in a parallel-wall channel. Observed similarities and differences be-

tween the droplet and hard-sphere systems elucidate the hydrodynamic phenomena governing the imbibition dynamics.

2 Materials and methods

2.1 Microfluidic device fabrication

The flow-focusing device $^{46-48}$ for preparation of monodisperse oil-in-water emulsions was fabricated using soft lithography techniques 49 from a silicon wafer mold. The width and length of the device orifice were $20\,\mu\mathrm{m}$ and $70\,\mu\mathrm{m}$, respectively, and the channels were $50\pm0.4\,\mu\mathrm{m}$ in height. To make hydrophilic channels, the PDMS-based chips were cut and punched with $500\,\mu\mathrm{m}$ biopsy punchers (Miltex) and bonded to glass slides (Fisher Scientific) by plasma bonding. The channels were then treated with water to maintain their hydrophilicity. Glass capillaries used for imbibition experiments were ordered from VitroCom. The capillaries were 5 cm long and made of borosilicate. All capillaries had the width-to-height aspect ratio w/h=10 and were purchased in two different sizes of $h=50\,\mu\mathrm{m}$ and $h=100\,\mu\mathrm{m}$.

2.2 Emulsion preparation

Monodisperse oil-in-water emulsions were prepared using 2 wt% aqueous solution of sodium dodecyl sulfate (SDS) (Sigma Aldrich) as the continuous phase and bromohexadecane (Sigma Aldrich) as the dispersed phase. The 2 wt% SDS corresponds to 8.6 times the critical micelle concentration. ⁵⁰ The addition of the SDS is necessary to prevent droplet coalescence. The interfacial tension between bromohexadecane and SDS, $\sigma = 0.11\,\text{mN/m}$, was determined using the pendant drop method. The density of the dispersed phase, 0.999 g/ml at 25°C, is close to water, so droplets are neutrally buoyant. Syringe pumps (PHD 2000, Harvard Apparatus) along with 1 ml plastic syringes were used to pump the fluids into the flow-focusing device. Bromohexadecane was pumped through the center channel and then sheared in the orifice by SDS solution flowing from the side channels.

Stock emulsions were prepared with two different droplet diameters, $d=60\,\mu\mathrm{m}$ and $d=65\,\mu\mathrm{m}$, both with $\phi=0.50$ oil volume fraction. The emulsions were then stored in microcentrifuge tubes (Fisher Scientific) and diluted to $\phi=0.4,0.3,0.2$, and 0.1 by adding 2 wt% SDS solution.

2.3 Imbibition experiments

The imbibition experiments in high aspect ratio microfluidic channels (Fig. 1(a)) were performed for two system geometries: strongly and moderately confined. In the strongly confined case an emulsion of $d=60~\mu\mathrm{m}$ diameter drops was imbibed into a capillary of height $h=50~\mu\mathrm{m}$. Since the drop diameter was larger than the channel height (d/h=1.2), the strongly confined drops were deformed to a disk-like shape after entering the channel. In the moderately confined system, the drop diameter and the channel height were $d=65~\mu\mathrm{m}$ and $h=100~\mu\mathrm{m}$, respectively (d/h=0.65). Under the experimental conditions, moderately confined drops remained nearly spherical and formed a monolayer close to the channel midplane. There were no significant overlaps of drop images (except for the closely packed regions), which corroborates that the drops formed a monolayer.

Page 3 of 21 Soft Matter

Observations of the imbibition process were conducted using five volume fractions of the bulk emulsion, 0.1 to 0.5. The system was imaged at either the entrance location 1 or the mid-channel location 2, as indicated in Fig. 1(a). A list of experiments and additional experimental details are provided in ESI.

To start an imbibition experiment, capillary tubes were placed on a glass slide. Emulsion stock was mixed by pipetting up and down to ensure homogeneity, then $500\,\mu\mathrm{m}$ of emulsion was drawn and carefully released near the capillary entrance. The released emulsion wetted the glass slide and imbibed into the capillary as soon as it reached its entrance. To avoid inertial effects from drop release or obscuring the images of the capillary entrance, the emulsion was not released directly on the entrance.

2.4 Dimensionless numbers

The Reynolds number Re and the capillary number Ca for our system are defined as Re = $\rho uh/\mu$ and Ca = $\mu u/\sigma$, where μ is the viscosity of the suspending fluid, ρ is its density, σ is surface tension, and u is the meniscus velocity.

For a capillary with height $h=50\,\mu\mathrm{m}$, we have $\mathrm{Re}\approx 1$ at location 1 and $\mathrm{Re}\approx 0.3$ at location 2. The corresponding values for $h=100\,\mu\mathrm{m}$ are $\mathrm{Re}\approx 2$ and $\mathrm{Re}\approx 0.6$. These values were evaluated when the meniscus was in the middle of the field of view. According to the above values, inertial effects are relatively small, but can produce lift forces 39 that drive moderately confined droplets towards the midplane of the capillary. Otherwise, the system is dominated by viscous forces, and Stokes-flow conditions approximately apply.

The capillary number Ca was smaller than 0.1 in all experiments. Our images show that the droplets inside the capillary were only weakly deformed by the flow. For d/h>1 they were flattened between the top and bottom channel walls to a disk-like shape, and for d/h<1 they remained nearly spherical. We note that, in addition to the inertial forces, small-deformation effects for moderately confined spherical droplets may also contribute to lift forces centering the drops in the channel. 43,51,52

2.5 Image processing

The acquired images were processed using a custom MATLAB (R2020a) program to determine the positions of the droplets and the meniscus. Prior to the imbibition process, a background image of the field of view was recorded. Since the droplet boundaries and the menisci appear as dark pixels, experimental frames and background image were inverted prior to background subtraction. Subtracted images were converted to binary images with a threshold chosen to remove noise. The coordinates of the center of the meniscus were used as its position.

To find the centroids of the droplets, the images were thresholded and the connected regions determined using the BWCONNCOMP function from the MATLAB (R2020a) image processing toolbox. A connected highly circular region with a size comparable to a droplet size was identified as a potential droplet. The centroids of individual droplets were used to extract their trajectories. We created a custom MATLAB (R2020a) code that uses a Kalman filter⁵³ and the Hungarian algorithm⁵⁴ for mul-

tiple object tracking. The extracted tracks were inspected and faulty tracks removed. The data generated by the MATLAB program were verified for random samples by comparing the image processing results to manual measurements performed using the IMAGEJ software package.

2.6 Area fraction measurements

The volume fraction of drops in the capillary differs from the bulk volume fraction because of entrance effects, different flow rates of the droplets and the continuous-phase fluid, and non-homogeneous droplet distribution in the original emulsion due to creaming. Therefore, drop concentration was directly measured in the capillary during the imbibition process.

Since our system is quasi-2D, the concentration is quantified using the area fraction $\phi_a=\frac{\pi}{4}d_\perp^2n$ of the drop monolayer inside the capillary. Here d_\perp is the radius of the drop projection onto the imaging plane, and n is the number of drops per unit area, determined by counting drops in the recorded images. For a system of moderately confined drops of diameter $d=65~\mu\mathrm{m}$ at the confinement ratio d/h=0.65, the projected diameter is $d_\perp=d$ because drops are nearly spherical. For the flattened strongly confined drops of diameter $d=60~\mu\mathrm{m}$ at the confinement ratio d/h=1.2, we find $d_\perp=72~\mu\mathrm{m}$ from our images.

To determine the area fraction of droplets in small subregions of a recorded image, we used an alternative method to bypass difficulties associated with counting droplets on the boundary between two subregions. We applied image processing techniques to fill the droplet interiors and count the number of pixels that the droplets encompass. This count was divided by the size of the subregion. Since the calculated area fractions were sensitive to some of the image-processing parameters, the parameter values were tuned to obtain results consistent with the area fraction determined for the entire region by drop counting.

2.7 Spatial and temporal coarse-graining of the area frac-

To determine the area fraction values ϕ_a , we employ several coarse-graining procedures, depending on the phenomena studied and the particle distribution. The local values of ϕ_a reported in Figs. 1(c), 1(f), and A.1 were obtained as averages computed within the small boxes depicted by blue vertical lines. In plots of the normalized imbibition time (Figs. 1(d) and 1(g)) and the linear transport coefficients (Figs. 2, 3, and 8) the area fraction values are averaged across both the spatial and temporal domains, using multiple images recorded in a given experiment.

2.8 Imbibition time and imbibition rate measurements

For experiments recorded at the entrance location 1, the imbibition time $t_{\rm fill}$, the time to fill the entire capillary, was determined as the time between forming the meniscus at the capillary inlet and the ceasing of droplet motion when the meniscus reached the end of the capillary. For experiments recorded at the mid-channel location 2, only the time interval between the meniscus arrival at the imaged region and termination of droplet motion could be observed. To evaluate the imbibition time $t_{\rm fill}$, we combined the

Soft Matter Page 4 of 21

directly measured interval with the estimated time the meniscus needs to reach location 2, obtained from Washburn scaling.³

The volumetric emulsion velocity \bar{u} was determined from the meniscus velocity, and the particle-phase velocity \bar{U} was evaluated in two ways. For a highly confined system (d/h=1.2), \bar{U} was obtained by measuring the velocity of the front between the emulsion and clear-fluid region. For a moderately confined system (d/h=0.65), where such front does not exist, \bar{U} was obtained by particle tracking, but this required low drop area fractions.

2.9 Evaluation of the capillary pressure

Since the contact angle and meniscus curvature are not directly observable in our experiments, the capillary pressure P_c was obtained from the imbibition rate of 2 wt% SDS solution. The penetration length L_0 and meniscus velocity \bar{u}_0 were measured either at location 1 or 2, and the capillary pressure was calculated from

$$P_c = \frac{L_0 \bar{u}_0}{v_0^{pp}},\tag{1}$$

where

$$v_0^{pp} = \frac{1}{12}\mu^{-1}h^2 \tag{2}$$

is the channel permeability coefficient.

For highly confined drops, a clear-fluid region exists next to the meniscus (Secs. 3 and 5), and the capillary pressure driving the emulsion imbibition is that of the clear fluid. For moderately confined drops, there is a dense suspension region next to the meniscus (Secs. 3 and 6), and drop interactions with the continuous-phase fluid interface can affect the capillary pressure. However, based on the data reported for the interfacial tension in Pickering emulsions, ⁵⁵ we expect that this effect is relatively small.

2.10 Simulations

To elucidate the observed droplet dynamics, we performed numerical simulations of a simplified system in which the droplets interact via the leading-order Hele–Shaw dipolar scattered flow fields, ^{40,56,57} and the near-field effects are modeled using a shortrange pairwise-additive repulsive potential (which prevents particle overlap). Previously, similar techniques were used for systems interacting via dipolar, ^{34,36} quadrupolar, ³⁷ and combined dipolar and quadrupolar ⁴³ flows produced by the particles. To replicate the effect of side walls, we used a flow-reflection method. ^{58,59}

For macroscopically homogeneous systems, periodic boundary conditions in the flow direction were applied. The leading portion of an inhomogeneous suspension was simulated explicitly, and the trailing region was modeled using a soft repulsive potential acting in the flow direction and moving with the suspension velocity. In strongly confined systems (with a clear-fluid region in front of the suspension region), modeling of the meniscus was not needed. At weaker confinements, particles accumulate behind the meniscus, which limits their forward motion. Thus, the effect of meniscus was represented by a short-range repulsive potential restricting particle positions to the behind-the-meniscus region.

2.11 Parameters of the cluster-migration model

In all theoretical calculations presented in Figs. 12 and 13 we use $\phi_{a2}=0.9$ for the area fraction of the clusters, $\chi_{c1}=1.25$ and $\chi_{c2}=1.1$ for the convective transport coefficient in the dilute and cluster regions, and $\varepsilon=0.4$ for the permeability-coefficient ratio (43). See the analysis provided in Secs. 6.2 and 6.4.

3 Key experimental observations

Figure 1 shows our key experimental observations for a highly confined system with d/h = 1.2 (panels (b)-(d)) and a moderately confined system with d/h = 0.65 (panels (e)-(g)). The confinement ratio d/h affects not only the drop shape but also the imbibition rate and drop distribution.

In the strongly confined case (d/h=1.2), two distinct regions develop during the imbibition: a droplet-free region behind the meniscus, followed by a suspension region (Fig. 1(*b*)). This behavior indicates that strongly confined disk-like droplets move slower than the continuous-phase fluid. In contrast, moderately confined spherical droplets (d/h=0.65) flow faster than the continuous phase; they catch up with the meniscus and create an adjacent dense droplet band (Fig. 1(*e*)).

The formation and decay of droplet clusters results in significant local area-fraction fluctuations for each confinement ratio (Fig. 1(c) and 1(f)). However, fluctuations for strongly confined drops are less pronounced than fluctuations at moderate confinement, and the clusters are usually smaller. Moreover, at strong confinement there is no systematic density gradient in the suspension region and the suspension and clear-fluid domains are separated by a sharp suspension front (Fig. 1(b) and (c)). In contrast, at the weaker confinement the drop area fraction gradually varies throughout the entire observation window, and there is no sharp front between the close-packed region next to the meniscus and the suspension behind it (Fig. 1(e) and (f)).

In Fig. 1(d) and (g) we characterize the imbibition rate by the time $t_{\rm fill}$ needed to fill the entire capillary (see Sec. 2.8 for measurement details). The time $t_{\rm fill}$ is normalized by the imbibition time for a clear continuous-phase fluid. Imbibition-time data indicate that drops increase the hydrodynamic resistance, increasing the imbibition time. This increase is more pronounced at the stronger confinement. For highly confined drops the results obtained from data collected at locations 1 and 2 agree. This agreement is consistent with the fact that use of the Washburn analysis to estimate the meniscus arrival time at location 2 (Sec. 2.8) is valid for this system, in spite of the presence of the clear-fluid and suspension regions (as demonstrated in Sec. 5.2). At moderate confinement, location 2 yields lower values of $t_{\rm fill}$ than location 1 because of the inaccuracy of the Washburn scaling in a highly non-uniform system. Moreover, drop area-fraction fluctuations cause t_{fill} to vary more from experiment to experiment.

4 Effective medium description of suspension transport in a channel

Our experimental results (Fig. 1) indicate that the difference between the overall emulsion velocity and the velocity of the dispersed phase affects the system dynamics in a nontrivial way. To Page 5 of 21 Soft Matter

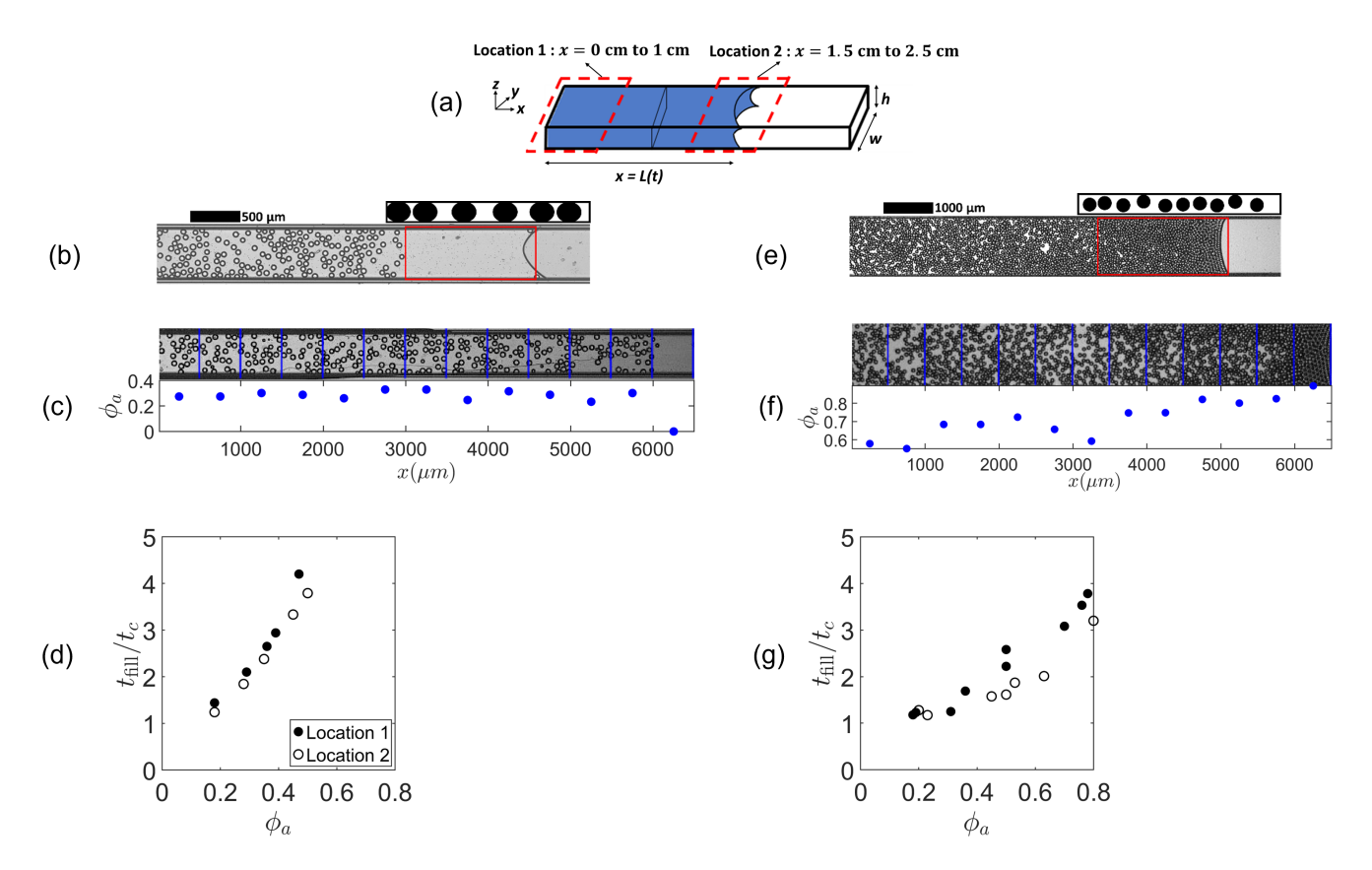


Fig. 1 Imbibition of strongly confined and moderately confined emulsions into a parallel-wall channel. (a) System schematic: Glass capillaries 5 cm long with an aspect ratio h/w=0.1 imbibe an oil-in-water emulsion. Images are recorded at location 1 or location 2 (as indicated). L(t) denotes the penetration length of the meniscus at time t. Representative experimental results for (b)-(d) highly confined droplets (drop diameter $d=60~\mu$ m and capillary height $h=50~\mu$ m) and (e)-(g) moderately confined droplets (drop diameter $d=65~\mu$ m and capillary height $h=100~\mu$ m). The images show the top view of the channel. As illustrated in the side-view schematics, highly confined droplets deform into a disk-like shape after entering the channel (b), whereas moderately confined droplets remain spherical (e). Highly confined flattened droplets move slower than the continuous phase, and a droplet-free region forms behind the meniscus (b); the area fraction ϕ_a in the emulsion region fluctuates but does not show a systematic spatial variation (c); the imbibition time $t_{\rm fill}$ increases with the increasing area fraction (d). Moderately confined spherical droplets flow faster than the continuous phase, and they form a densely packed droplet band behind the meniscus (e); the area fraction ϕ_a fluctuates and shows a systematic increase in the flow direction (f); the imbibition time increases with the area fraction and strongly fluctuates from experiment to experiment (g). The graphs in panels (c) and (f) present the area fraction averaged over the zones marked by blue lines in the corresponding images. The imbibition time $t_{\rm fill}$ in (d) and (g) is normalized by the imbibition time $t_{\rm c}$ for the clear suspending fluid in a channel of the same geometry.

quantify the emulsion and drop fluxes during the imbibition process, we use quasi-2D effective-medium transport equations, ^{33,57} formulated here for the flow component along the channel.

The emulsion transport is described by the volumetric emulsion velocity \bar{u} and the particle-phase velocity \bar{U} , both of which are coarse-grained and averaged across the channel height h. The particle-phase flux $\phi_a \bar{U}$ obeys the continuity relation

$$\frac{\partial \phi_a}{\partial t} = -\nabla_{\parallel}(\phi_a \bar{U}),\tag{3}$$

and the velocity \bar{u} satisfies the incompressibility condition

$$\nabla_{\parallel}\bar{u} = 0. \tag{4}$$

Here ∇_{\parallel} denotes the gradient operator in the flow direction, and unidirectional flow (or flow averaged over the channel width w) is assumed.

The velocities \bar{U} and \bar{u} are driven by the local pressure gradient $\nabla_{\parallel} p$ generated by the capillary pressure of the meniscus P_c .

The dependence of the local velocities on the driving pressure is described by the constitutive relations

$$\bar{U} = -v^{tp} \nabla_{\parallel} p, \tag{5a}$$

$$\bar{u} = -v^{pp} \nabla_{\parallel} p, \tag{5b}$$

which involve two transport coefficients: the particle-phase mobility v^{tp} and the effective permeability of the channel to the suspension flow v^{pp} .

In addition to the constitutive relations (5) that characterize the response of the system to the applied pressure gradient, we also introduce the transport relation

$$\bar{U} = \chi_c \bar{u} \tag{6}$$

that describes particle convection by the average flow. According to the above equations, the particle-phase mobility coefficient v^{tp} , the effective permeability coefficient v^{pp} , and the convective

Soft Matter Page 6 of 21

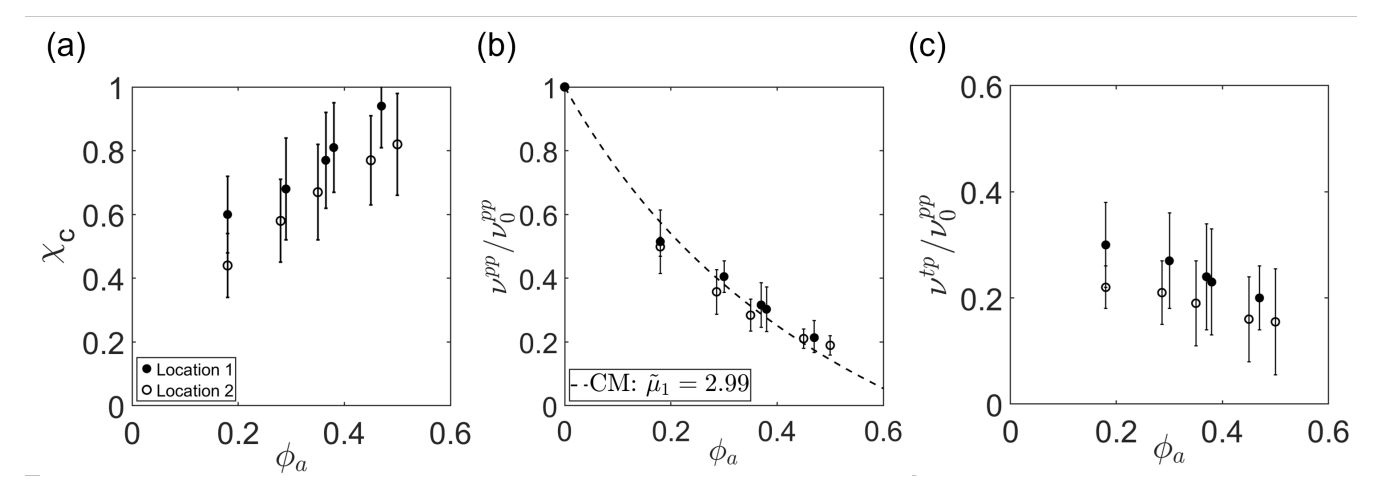


Fig. 2 Transport coefficients for strongly confined disk-like droplets. (a) The convective transport coefficient χ_c , (b) effective permeability coefficient v^{pp} , and (c) droplet-phase mobility coefficient v^{tp} shown vs the area fraction ϕ_a for the strongly confined system (d/h = 1.2). The results for v^{pp} and v^{tp} are normalized by the transport coefficients v_0^{pp} for the clear suspending fluid in the channel of the same geometry. The results obtained from measurements at locations 1 and 2, as labeled. The dashed line in panel (b) represents the Clausius-Mossotti approximation (22) with $\tilde{\mu}_1 = 2.99$.

transport coefficient χ_c are related,

$$v^{tp} = \chi_c v^{pp}. (7)$$

For a clear (drop-free) continuous-phase fluid, the permeability coefficient in relation (5b) is given by eqn (2). The transport coefficients v^{tp} , v^{pp} , and χ_c depend on the channel height h, confinement ratio d/h, area fraction ϕ_a , and flow-induced local drop distribution. Transport coefficients are also affected by the emulsion flow rate, because the drop-wall friction depends on the drop velocity. $^{60-63}$ As discussed in Sec. 5.3, our measurements are consistent with a moderate flow-rate dependence.

5 Imbibition of strongly confined disk-like droplets

5.1 General observations

In this section we use the effective-medium equations (3)–(6) to elucidate hydrodynamic phenomena observed during imbibition of strongly confined disk-like droplets. We demonstrate the validity of Washburn scaling, measure the transport coefficients, analyze the formation of a suspension front, and explain the microstructural fluctuation dynamics.

Since the imbibition flow is driven by the pressure drop

$$\Delta p = P_c \tag{8}$$

generated by the capillary pressure P_c , many features observed in our experiments are similar to those reported for a strongly confined drop monolayer flowing due to applied pressure in a microfluidic parallel-wall channel. ³⁴ These phenomena include a sharp suspension front, propagation of density waves, and strong drop velocity fluctuations. The previous experiments and analysis focused, however, only on the particle-phase dynamics. ³⁴ We show that both the particle phase motion and volumetric suspension motion are important for the imbibition process. Here we generalize the previous results by using a more complete descrip-

tion provided by the transport equations (3)–(6). In addition to the two-phase effective-medium theory, we employ a dipolar simulation model and a mobility analysis of particle clusters to relate the observed microstructural features to the measured large velocity fluctuations.

5.2 Channel resistance and the validity of Washburn scaling

To determine how the total penetration length L varies with time during imbibition of a strongly confined emulsion, we first note that the meniscus velocity $\mathrm{d}L/\mathrm{d}t$, the volumetric emulsion velocity \bar{u} , and the clear-fluid velocity \bar{u}_c are the same,

$$dL/dt = \bar{u} = \bar{u}_c, \tag{9}$$

by the incompressibility condition. Similarly, the velocity of the front between the uniform-suspension domain and clear-fluid domain equals the particle-phase velocity,

$$dl_s/dt = \bar{U}, \tag{10}$$

where l_s is the length of the suspension region in the channel. Thus, the convective transport relation (6) implies that

$$dl_s/dt = \chi_c dL/dt. \tag{11}$$

Upon integrating eqn (11) with the initial condition $l_s = L = 0$, we obtain

$$l_s/L = \chi_c \tag{12a}$$

and

$$l_c/L = 1 - \chi_c, \tag{12b}$$

where $l_c = L - l_s$ is the length of the clear-fluid region. Accordingly, the fractions of the filled portion of the channel that are occupied by the suspension and by the clear fluid do not change as the imbibition process progresses.

Equations (12) imply that the channel resistance R, defined by

Page 7 of 21 Soft Matter

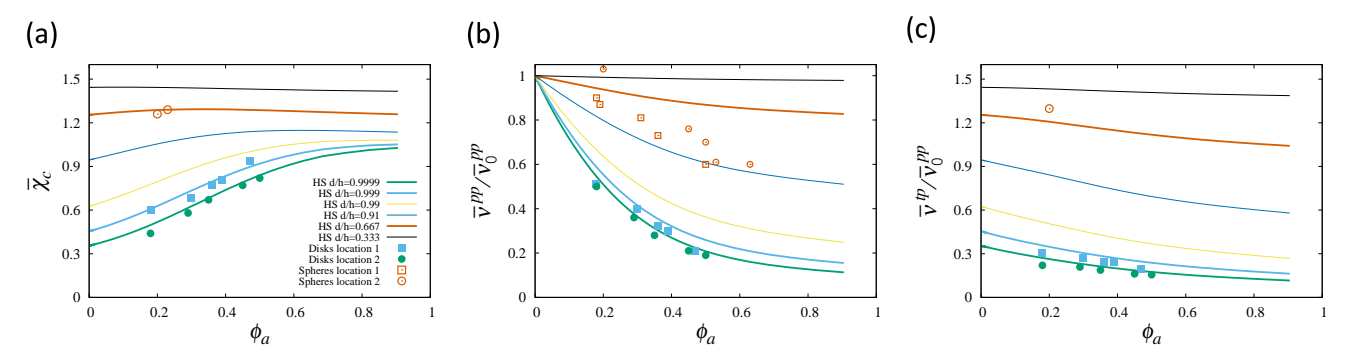


Fig. 3 Mapping of experimental transport coefficients onto theoretical hard-sphere (HS) results. (a) The convective transport coefficient χ_c , (b) normalized effective permeability coefficient v^{pp} , and (c) normalized particle-phase mobility coefficient v^{tp} , shown vs the area fraction ϕ_a . Experimental results for highly confined disk-like droplets (filled symbols) and moderately confined spherical drops (open symbols) were obtained at locations 1 and 2 (as labeled). Solid lines represent theoretical calculations for a hexagonal monolayer of rigid spheres in the midplane of the channel for different values of d/h (as labeled). For highly confined droplets, the experimental measurements at location 1 (blue) and location 2 (green) agree well with the hard-sphere results for d/h = 0.999 and d/h = 0.999 respectively. In this range of very small particle—wall gaps $\varepsilon = 1 - d/h$, the adjustment of d/h affects only the particle—wall lubrication friction, without changing other contributions to the hydrodynamic friction matrix. For spherical droplets at confinement ratio d/h = 0.65 (red) experimental measurements at low area fractions agree well with the hard-sphere theory for the same value of d/h. At higher area fractions, the experimental results are available only for v^{pp} averaged over coexisting low- and high-density regions. The measured average values are below the theoretical prediction because of drop displacements from the channel midplane in high-density domains.

the linear relation

$$\Delta p = R\bar{u} \tag{13}$$

between the pressure drop Δp and the volumetric emulsion velocity \bar{u} , is proportional to the penetration length L, similar to the case of imbibition of a single-phase homogeneous fluid. Namely, since the clear-fluid region is followed by the suspension region, the channel resistance is a sum of the resistance coefficients for the clear-fluid and suspension segments,

$$R = \frac{l_c}{v_0^{pp}} + \frac{l_s}{v^{pp}},\tag{14}$$

where v_0^{pp} and v^{pp} are the channel permeability coefficients in clear-fluid and suspension domains, respectively.

Based on relations (12), the channel resistance (14) is

$$R = L/v_{\text{eff}}^{pp} \tag{15}$$

where

$$\frac{1}{v_{\rm eff}^{pp}} = \frac{1 - \chi_c}{v_0^{pp}} + \frac{\chi_c}{v^{pp}} \tag{16}$$

is the inverse effective permeability coefficient, which depends only on the transport coefficients in the suspension and clear-fluid regions. Combining eqns (9), (13), and (15) and using eqn (8) for the pressure drop Δp , we obtain the differential equation

$$LdL/dt = V_{\text{off}}^{pp} P_C, \tag{17}$$

which, upon integration, yields

$$L^2 = 2v_{\rm eff}^{pp} P_C t. \tag{18}$$

Relation (18) shows that the Washburn scaling $L^2 \sim t$ holds for highly confined drops, despite formation of suspension and clear-fluid regions during imbibition.

5.3 Evaluation of transport coefficients

The results of Sec. 5.2 can be used to extract the values of transport coefficients from our experimental data for the meniscus and suspension front motion. The convective transport coefficient χ_c is evaluated by using eqns (9) and (10) to determine the continuous-phase and particle-phase velocities \bar{u} and \bar{U} from the measurements of the meniscus and suspension-front positions. The permeability coefficient v^{pp} is obtained using expression

$$\frac{v^{pp}}{v_0^{pp}} = \frac{l_s}{l_{0c} - l_c},\tag{19}$$

where

$$l_{0c} = \frac{v_0^{pp} P_c}{\bar{u}} \tag{20}$$

(see eqns (8), (13), and (14)). The length l_{0c} can be interpreted as the penetration length for which the clear fluid in a single-phase experiment moves with the same velocity \bar{u} as the velocity measured during the emulsion imbibition process. Combining expression (1) and (20) yields

$$l_{0c} = \frac{L_0 \bar{u}_0}{\bar{u}}.\tag{21}$$

After evaluating the transport coefficients χ_c and v^{pp} , the particle-phase mobility v^{tp} is obtained using eqn (7).

5.4 Area-fraction dependence of the transport coefficients

The measured values of the transport coefficients are presented in Fig. 2 vs the drop area fraction ϕ_a in the suspension region. The transport coefficient χ_c is dimensionless, and both v^{pp} and v^{tp} are normalized by the channel permeability coefficient for the particle-free continuous-phase fluid v_0^{pp} in the same capillary.

The results in Fig. 2(a) show that the convective transport coefficient χ_c increases with ϕ_a . In the area-fraction region where the measurement results are available, the increase is approximately linear, and at the highest available value $\phi_a \approx 0.5$ we have

Soft Matter Page 8 of 21

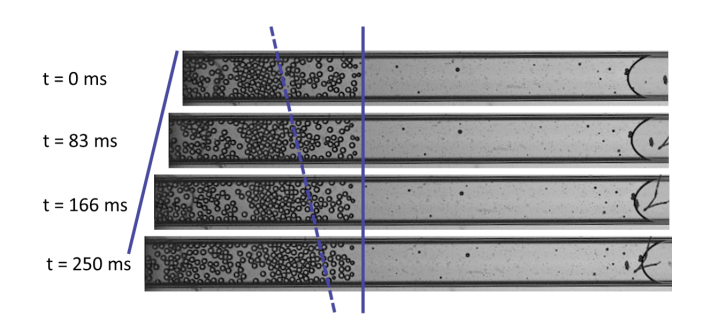


Fig. 4 Density wave propagation during the imbibition of disk-like droplets. A sequence of time-lapse images of an emulsion of highly confined drops (d/h=1.2 and area fraction $\phi_a=0.35)$ showing a propagating density wave. The images are shifted and aligned on the suspension front as indicated by the solid lines. The leading edge of the density wave is marked by the tilted dashed line. The line slope shows that the wave that gradually approaches the suspension front moves faster than the drop phase, consistent with the predicted wave velocity (28).

 $\chi_c \approx 0.9$. For larger area fractions, we expect that χ_c saturates at a value close to 1, as argued in Sec. 5.4.2.

According to Fig. 2(*b*) and Fig. 2(*c*), the permeability coefficient v^{pp} and drop-phase mobility coefficient v^{tp} are both decaying functions of the area fraction ϕ_a . However, the decay of v^{pp} is much more pronounced. At small values of ϕ_a , the coefficient v^{pp} is significantly larger than v^{tp} , but at higher area fractions v^{tp} and v^{pp} approach approximately the same value, consistent with the behavior of $\chi_c = v^{tp}/v^{pp}$ seen in Fig. 2(*a*).

5.4.1 Clausius-Mossotti approximation

The dashed line in Fig. 2(b) represents the generalized Clausius–Mossotti approximation

$$\frac{v_{\text{CM}}^{pp}}{v_0^{pp}} = \frac{1 - \frac{1}{2}\tilde{\mu}_1}{1 + \frac{1}{2}\tilde{\mu}_1},\tag{22}$$

originally proposed by Blawzdziewicz and Wajnryb, 57 based on the analogy between microscale transport equations governing suspension flow in a Hele–Shaw cell and the 2D effective dielectric-constant problem. The low-density expansion coefficient $\tilde{\mu}_1$ in eqn (22) is estimated by fitting the overall areafraction dependence of v^{pp} to avoid errors associated with inaccuracies of individual low-density points. We find that the Clausius–Mossotti approximation (22) agrees with the experimental data within the experimental error.

5.4.2 Moving-permeable-medium model

Important insights into the behavior of the transport coefficients χ_c , v^{pp} , and v^{tp} at high drop concentrations can be gained by considering a moving-permeable-medium model. In this approximation, the particle phase is treated as a porous medium translating in the channel with velocity \bar{U} . The continuous-phase fluid moves together with this medium; in addition, the fluid percolates through it under the action of the pressure gradient. The macroscopic emulsion velocity can thus be expressed as

$$\bar{u} = \bar{U} + \bar{\mu}_s \nabla_{\parallel} p, \tag{23}$$

where the second term is the medium permeability contribution with $\bar{\mu}_s$ denoting the normalized permeability coefficient. The velocity of the permeable-medium motion is given by the friction relation

$$\nabla_{\parallel} p = f \bar{U}, \tag{24}$$

where $f = 1/v^{tp}$ is the friction coefficient.

Taking into account constitutive relations (5), eqn (23) yields

$$v^{pp} = v^{tp} + \bar{\mu}_s. \tag{25}$$

The corresponding expression for the convective transport coefficient χ_c is

$$\chi_c = \frac{v^{tp}}{v^{tp} + \bar{\mu}_s}.$$
 (26)

Since the porous-medium permeability $\bar{\mu}_s$ rapidly decreases towards zero at high area fractions of the dispersed phase, the dropphase velocity \bar{U} and suspension velocity \bar{u} are nearly the same for large values of ϕ_a . Thus, the difference between v^{pp} and v^{tp} is small, according to eqn (25). Correspondingly, the convective transport coefficient χ_c increases with the increasing area fraction and then saturates assuming values close to unity. These conclusions are consistent with the results shown in Fig. 2 and with hard-sphere results discussed in Sec. 5.5.

The moving-permeable-medium model also helps explain why the measurements at location 1 (close to the entrance of the capillary) tend to yield higher values of the transport coefficients χ_c , v^{pp} , and v^{tp} than the measurements at location 2. The observed location dependence results from a decreased droplet-wall lubrication friction due to higher flow velocity at location 1. Such velocity dependence stems from an increase in the thickness of the film separating the drop from the walls, as predicted by Bretherton analysis 64 and observed in microfluidic experiments 62 and numerical simulations. 60 The decreased friction coefficient f results in the corresponding increase of the particle-phase mobility v^{tp} . As a consequence, the coefficients v^{pp} and χ_c also increase, according to eqns (25) and (26). Other nonlinear effects not accounted for in our analysis (such as inertial effects and the evolution of particle distribution) may also affect the transport coefficients, contributing to their position dependence.

5.5 Mapping between transport coefficients of the highly confined emulsion and a hard-sphere monolayer

As suggested by the moving-permeable-medium model, physical mechanisms governing the particle-phase and continuous-phase motion are general; they are valid not only for a confined emulsion flow but also for a flow of a hard-sphere monolayer. Moreover, since the surfactant present in the experimental system partially immobilizes drop interfaces by suppressing compressible surface velocity components, ⁶⁵ fluid flow through drop and hard-sphere arrays is expected to be similar. The main difference between the emulsion and hard-sphere monolayers is in the particle–wall hydrodynamic friction. For disk-like droplets, the particle–wall friction is generated in the thin fluid film between the wall and the flattened drop interface. For highly confined rigid spheres, the friction is produced in the lubrication layer in

Page 9 of 21 Soft Matter

a much smaller near-contact region. However, the friction can be approximately matched between the two systems by adjusting the dimensionless particle–wall gap $\varepsilon = 1 - d/h$ for hard spheres.

Figure 3 compares the emulsion transport coefficients measured in the imbibition experiments with benchmark calculations for a confined hard-sphere monolayer driven by a pressure gradient in a parallel-wall channel. The benchmark calculations were carried out using the Cartesian representation method 41 for a hexagonal lattice moving in the midplane of the channel. For details of our technique along with a theoretical analysis of particle transport in parallel-wall channels see our earlier study. 57

We find that for an appropriate choice of the particle wall gap ε , the measured transport coefficients for disk-like droplets agree with the corresponding theoretical hard-sphere calculations. Specifically, the measurements performed at locations 1 and 2 can be mapped onto the hard-sphere results with d/h=0.999 ($\varepsilon=0.001$) and d/h=0.9999 ($\varepsilon=0.0001$), respectively. For such strongly confined rigid spheres, the choice of the particle—wall gap ε sets the value of the particle—wall friction coefficient but, otherwise, does not affect hydrodynamic interactions in the system. Since for the longitudinal hard-sphere motion the particle—wall friction coefficient depends on ε logarithmically due to the small size of the near-contact region, we need to use $\varepsilon \ll 1$ to match the theoretical calculations to the experimental results for a suspension of flattened drops.

The particle—wall gap ε matching the data from location 1 is larger than the corresponding gap for location 2. This is consistent with lower drop—wall friction for smaller emulsion penetration lengths L, for which drops move faster and therefore fluid films separating them from the walls are thicker.

The quantitative agreement between the experiments and hard-sphere calculations allows us to predict the values of transport coefficients for systems where accurate measurements are not available. In particular, the hard-sphere simulations confirm our conclusion that at high area fractions the convective transport coefficient χ_c tends to a value close to unity. In Sec. 6 we will use hard sphere results to complement experimental measurements to facilitate our analysis of transport at a weaker confinement.

5.6 A sharp suspension front and density-wave propagation

During the capillary imbibition of disk-like droplets a sharp front forms between the suspension domain and droplet-free region (Fig. 1(*b*) and (*c*)), and the density fluctuations exhibit wavelike dynamics (Fig. 4). Both these phenomena can be understood based on the convective transport equation (6).

Since the transport coefficient χ_c is an increasing function of ϕ_a (Fig. 2 (a)), domains with higher area fraction move faster than lower-density regions. In a suspension zone where the area fraction decreases, (e.g., in the leading end of the suspension region), the higher-density portion catches up with the lower-density one. This results in sharpening of the area-fraction gradient and in the formation of a density front. Without such a front-sharpening mechanism, the transition between the suspension and clear-fluid regions would be gradual. For moderate amplitude density fluctuations, a similar mechanism produces forward-propagating den-

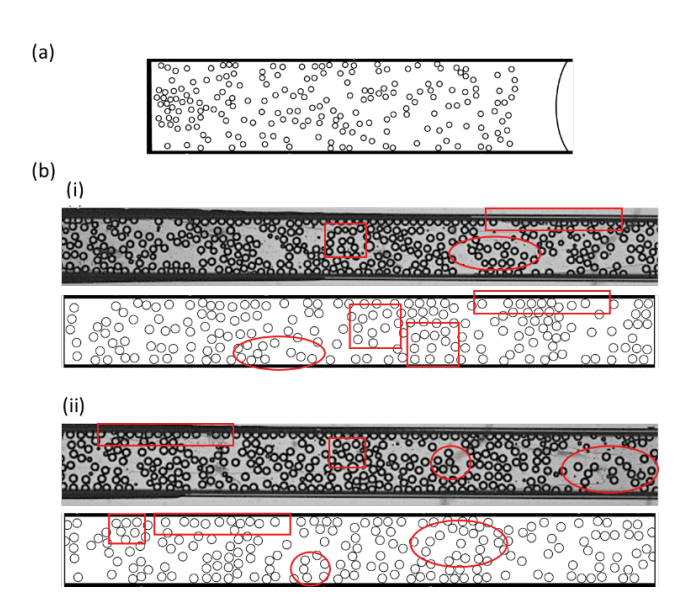


Fig. 5 Self-organized microstructural features in a highly confined emulsion. (a) Numerical simulation using dipolar model with near-field repulsion shows a sharp suspension front and short chain-like particle clusters, similar to those seen in experiments. The meniscus is drawn as a guide for the eye (b) A comparison between experimentally observed (top images) and simulated (bottom images) microstructural features. Similar structural elements are highlighted using contours of the same shape.

sity waves, because the leading end of the dense region collects particles from the slower low-density region in front of it.

A similar behavior observed in pressure-driven flow in a Hele–Shaw microfluidic channel was described in terms of the linear Burgers equation. ³⁴ Here we generalize these results for drop evolution in the imbibition process. By combining the continuity relation (3) and the convective constitutive relation (6), we obtain the generalized inviscid Burgers equation,

$$\frac{\partial \phi_a}{\partial t} = -c(\phi_a) \nabla_{\parallel} \phi_a, \tag{27}$$

where

$$c(\phi_a) = \left[\chi_c(\phi_a) + \phi_a \frac{\mathrm{d}\chi_c(\phi_a)}{\mathrm{d}\phi_a} \right] \bar{u}$$
 (28)

is the area-fraction-dependent velocity of density waves. The second term in eqn (28) represents the wave velocity relative to the particle-phase velocity given by the first term. In Ref. 34 only the linear relation between the suspension and particle velocities was considered, $\chi_c(\phi) = \chi_c(0) + \alpha \phi_a$, where α is the proportionality coefficient. Equations (27) and (28) generalize this result.

The Burgers equation (27) predicts the formation of density shocks between the high- and low-density regions for systems where the wave velocity $c(\phi_a)$ is an increasing function of the area fraction ϕ_a . This is the case in our experimental system. Shock formation can be demonstrated using the method of characteristics, and it results from the characteristics crossing. The observed sharp front between the suspension and clear-fluid regions is an example of a density shock predicted by the Burgers equation. ³⁴

We note that the wave velocity (27) is greater than the convective velocity (6). Thus, the density waves associated with spontaneously occurring density fluctuations propagate faster than the

Soft Matter Page 10 of 21

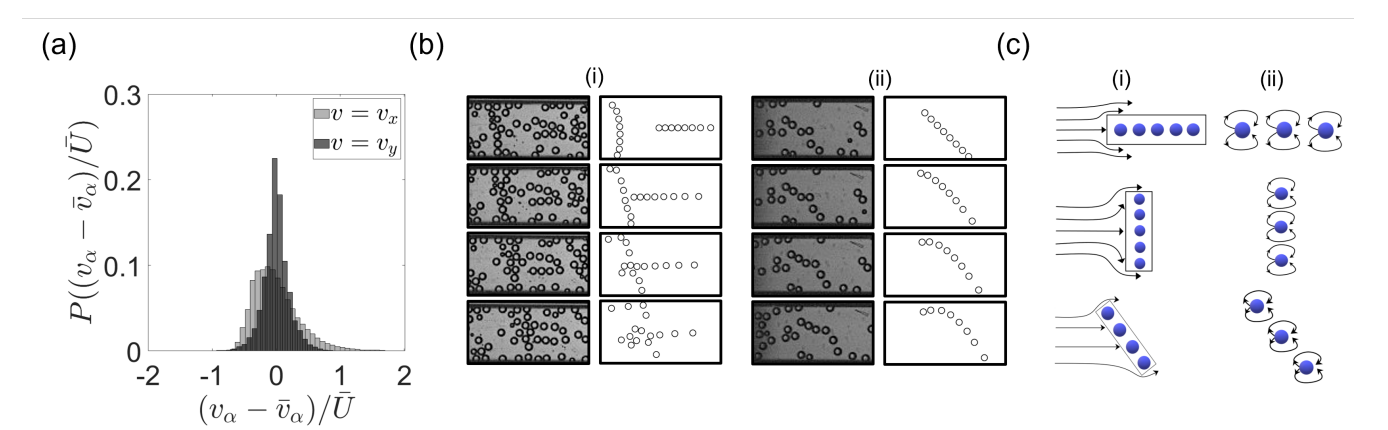


Fig. 6 Large velocity fluctuations in a strongly confined emulsion. (a) Experimentally measured distribution of the longitudinal (ν_x) and transverse (ν_y) drop velocity about the average value $\bar{\nu}_{\alpha}$ ($\alpha=x,y$) for $\phi_a=0.35$ and d/h=1.2. The velocity fluctuations are of the same order as the average drop-phase velocity \bar{U} . (b) Time-lapse video frames and qualitatively matching simulation images show that transversely oriented drop chains move faster than the longitudinally oriented ones (panels (ii)) and that diagonally oriented drop chains migrate in the transverse direction y (panels (ii)). The velocity differences generate large velocity fluctuations. (c) Schematic explaining the origin of the drop velocity dependence on chain orientation. Panels (i) show that external flow more easily bypasses a chain oriented parallel than the one oriented normal to the flow direction. Thus the flow pushes the chain more strongly in the direction normal to the chain, resulting in the orientation dependence of chain velocity. Panels (ii) show how hydrodynamic interactions via microscale dipolar flows produce chain migration.

average particle velocity and the suspension front (Fig. 4). A direct measurement of the wave velocity yields $c/\bar{u}=1.34$; the prediction $c/\bar{u}\approx 1.3$ from eqn (28) is consistent with this result.

The observed density-wave-propagation direction relative to the average particle velocity in the quasi-2D imbibition system is opposite to the one reported for 1-D drop trains. ³⁶ For linear chains oriented parallel to the flow direction, the particle mobility (equivalent to the convective transport coefficient χ_c) decreases with the increasing particle density per unit length. ⁶⁶ Equation (28) shows that the decrease of the mobility coefficient implies the backward direction of the propagating density wave relative to the average particle motion.

5.7 Self-organized droplet clusters and their dynamics

According to the experimental images (Figs. 5 and 6), droplets self-organize into a variety of local arrangements, which include short chains of different orientations (elongated or more compact) as well as high density regions separated by gaps of much lower particle density. Our dipolar-interaction simulation model (Sec. 2.10) captures the emergence of these transient structures (Figs. 5 and 6). It also reproduces the sharp border between the suspension and clear fluid regions (Fig. 5(a)). Since, apart from the axisymmetric near-field repulsion, particles in the model interact only via the Hele–Shaw dipoles, the agreement between the experimental and simulated microstructure shows that dipolar hydrodynamic interactions are the main organizing factor of the emerging microstructural dynamics. (A similar behavior was reported for strongly confined microfluidic emulsion flows. 34)

The chains generated during the imbibition are usually short, with a typical length of several particles. They have relatively short lifetime because of inherent chain instabilities (transverse ones at the trailing end and longitudinal ones at the leading end) 43 and collisions with other microstructural features. We note that isolated transverse chains are more stable 67 than lon-

gitudinal ones. 43 The microstructure generated during the imbibition is much less ordered than the one seen for a system of shear-driven deformable droplets 68 (with the dynamics governed by the Hele–Shaw quadrupolar interactions instead of dipoles). 37

As illustrated in the time-lapse sequence of video images presented in Fig. 6(b), chains and other elongated clusters with transverse orientation (across the channel) move faster than those longitudinally oriented. Fig. 6(b) also shows that diagonally oriented clusters have nonzero transverse velocity. As a result, particles exhibit large velocity fluctuations (Fig. 6(a)), whose magnitude is of the same order as the average particle velocity.

The variation in the velocity magnitude and direction of cluster motion stems from the geometry of dipolar backflow patterns (Fig. 6(c)); it can be semiquantitatively described by modeling a particle chain as an elongated rigid body. In this approximation, the chain velocity **V** is given by the mobility relation

$$\mathbf{V} = \mathbf{v}^c \cdot \mathbf{u},\tag{29}$$

where \mathbf{u} is the velocity of the incident flow, and

$$\mathbf{v}^c = \mathbf{v}_{\parallel}^c \hat{\mathbf{t}} \hat{\mathbf{t}} + \mathbf{v}_{\perp}^c \hat{\mathbf{n}} \hat{\mathbf{n}}$$
 (30)

is the mobility tensor. Here $\hat{\bf t}$ and $\hat{\bf n}$ are the unit vectors parallel and perpendicular to the chain, and v_{\parallel}^c and v_{\perp}^c are the longitudinal and transverse mobility components. Combining relations (29) and (30), we get the expressions

$$V_x = (v_{\parallel}^c \sin^2 \theta + v_{\parallel}^c \cos^2 \theta)u \tag{31a}$$

$$V_{y} = (v_{\perp}^{c} - v_{\parallel}^{c})\sin(2\theta)u \tag{31b}$$

for the longitudinal and transverse chain velocity components V_x and V_y , where θ is the angle between the flow direction $\hat{\mathbf{e}}_x$ and the normal to the chain $\hat{\mathbf{n}}$.

In strongly confined systems, the mobility tensor of a particle

Page 11 of 21 Soft Matter

chain or elongated cluster is strongly anisotropic, ^{42,66} with the transverse mobility much larger than the longitudinal mobility,

$$v_{\perp}^{c} > v_{\parallel}^{c}. \tag{32}$$

The large anisotropy stems from the fact that in a quasi-2D system the fluid cannot easily bypass a chain oriented normal to the flow direction. Thus, the chain is pushed forward and moves with the velocity close to the velocity of the incident flow. In contrast, a longitudinal chain can be more easily bypassed by the incident flow (Fig. 6(c)), and therefore, it moves slower.

Equation (31a) predicts that chains with approximately transverse orientation $\theta=0^\circ$ move faster along the channel than the longitudinal ones ($\theta=90^\circ$). For strongly confined chains of nearly touching particles, transverse mobility can be more than three times larger than the longitudinal one, ⁶⁶ leading to the velocity variation larger than the average chain velocity. Moreover, diagonally oriented chains ($0^\circ < \theta < 90^\circ$) have a nonzero transverse velocity, (eqn (31b)). Large velocity fluctuations and transverse cluster motion are observed both in experiments and numerical simulations (Fig. 6(a) and (b)).

The large velocity variation between clusters with different orientations causes formation of local void regions and generates high density domains associated with cluster collisions 6(b)). These confinement-induced phenomena contribute to the richness of the collective drop dynamics during emulsion imbibition under strong-confinement conditions.

6 Imbibition of moderately confined spherical droplets

6.1 General observations

The imbibition of a monolayer of spherical droplets differs considerably from the imbibition of strongly confined droplets discussed in Sec. 5. The difference stems from the magnitude of the convective transport coefficient χ_c . Moderately confined spherical droplets reside near the midplane of the channel and thus sample higher velocity streamlines. As a result, they move faster than the average suspension flow (i.e., $\chi_c > 1$) and form a dense droplet band behind the meniscus, as seen in Fig. 1(e) and 1(f).

Focusing of droplets towards the midplane can result from inertial migration ³⁹ and deformation-induced migration. ^{43,51,52} In our system, both the Reynolds number and capillary number are small. However, since the drop phase and continuous phase are density-matched, a small migration velocity is sufficient for drop centering, except for densely packed areas, where strong interparticle interactions result in significant drop displacements towards the lower and upper walls (Fig. 7).

We show that the highly packed region near the meniscus can either be disordered or include hexagonally packed ordered domains. This region is often unstable, continuously shedding high-density drop clusters, which affects drop dynamics upstream from the meniscus.

6.2 The effective transport coefficients

For strongly confined disk-like droplets, the existence of distinct uniform-suspension and clear-fluid regions allowed us to determine the coefficients χ_c , v^{pp} , and v^{tp} for a range of area fractions (Fig. 2). For spherical droplets, however, significant area-fraction nonuniformities in the imbibed emulsion (Fig. 1(e) and 1(f)) limit our ability to evaluate the transport coefficients. Thus, the results presented here are less complete than those given in Sec. 5.4.

6.2.1 Channel permeability coefficient v^{pp}

Evaluation of the transport coefficient v^{pp} requires measuring the volumetric suspension velocity \bar{u} and determining the local pressure gradient in a region of a given drop area fraction. While \bar{u} can be obtained from the meniscus velocity, the local pressure gradient cannot be evaluated from our experimental data because of the suspension nonuniformities. Therefore, we calculate the average value of v^{pp} for the entire channel,

$$v^{pp} = -\bar{u}/(\nabla_{\parallel}p)_{\text{avg}},\tag{33}$$

where

$$(\nabla_{\parallel} p)_{\text{avg}} = P_c/L \tag{34}$$

is the average pressure gradient generated by the capillary pressure P_c . As in the case of strongly confined disk-like drops, the capillary pressure is determined using clear-fluid experiments, on assumption that drop presence next to the meniscus does not significantly affect the contact angle and interfacial tension.

The average permeability coefficient v^{pp} is plotted in Fig. 8 vs the average area fraction. The data show that v^{pp} is a decreasing function of the area fraction, although the decay is slower than the corresponding decay for disk-like droplets (Fig. 2).

6.2.2 Convective transport coefficient χ_c

Evaluation of the convective transport coefficient χ_c requires measurements of the volumetric suspension velocity \bar{u} and the particle-phase velocity \bar{U} (eqn (6)). The velocity \bar{u} has been obtained from the motion of the meniscus, but \bar{U} is more difficult to measure because there is no suspension front moving with the velocity of the particle phase. For low-area fractions, \bar{U} can be evaluated by particle tracking, but at higher ones tracking is inaccurate. Thus, we provide results only for the low area fraction system, using data from location 2. Our particle-tracking measurements yield $\chi_c = 1.26$ for $\phi_a = 0.2$ and $\chi_c = 1.29$ for $\phi_a = 0.23$.

The above experimentally determined values are very close to the value $\chi_c^{\text{Faxen}} = 1.29$ that is obtained from Faxen's law ⁶⁹

$$\bar{U} = v + \frac{d^2}{24} \nabla^2 v \tag{35}$$

for a finite-size particle in the parabolic flow

$$v(z) = 6\frac{z}{h} \left(1 - \frac{z}{h}\right) \bar{u}. \tag{36}$$

The channel walls are at z=0 and z=h and the particle is placed in the middle of the channel. Equation (35) accounts for the finite particle size (for a point particle the result $\chi_c=1.5$ would be about 15% higher) but does not include particle–particle and particle–wall hydrodynamic interactions. The agreement be-

Soft Matter Page 12 of 21

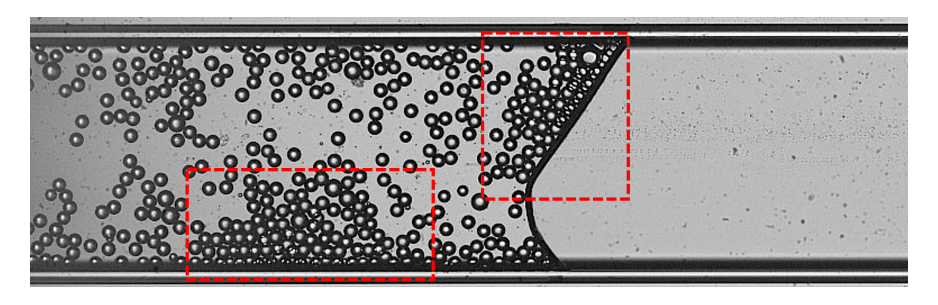


Fig. 7 Droplet displacement out of the channel midplane in highly packed regions. High magnification images (4X) of dense regions formed during the imbibition of spherical droplets upstream of the meniscus and at the meniscus. The drop images in the marked regions show overlapping boundaries, indicating the displacement of the droplets out of the midplane.

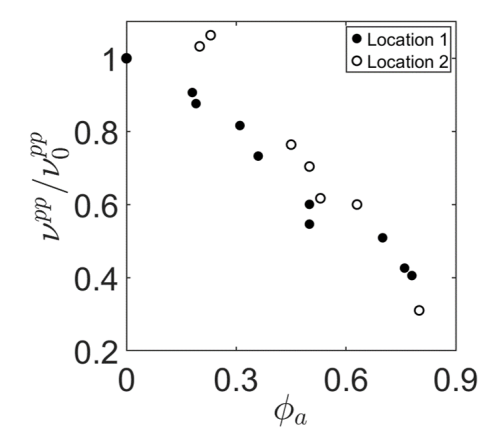


Fig. 8 The average effective permeability coefficient v^{pp} of a suspension of moderately confined spherical droplets vs the average area fraction ϕ_a . Confinement ratio d/h = 0.65; locations 1 and 2, as labeled. The average transport coefficient combines contributions from the high-density band next to the meniscus and the upstream lower-density region.

tween the Faxen's result (35) and the experimental values indicates that the effect of such interactions is relatively minor.

6.2.3 Hard-sphere mapping

Figure 3 shows that in the low area fraction regime the experimental data for v^{pp} and χ_c agree well with the hard-sphere calculations for a system with similar confinement ratio d/h. Flow modes with nonzero surface divergence are immobilized on the drop interfaces by the surfactant monolayer, 65 and this partial immobilization makes the droplet and hard-sphere systems hydrodynamically similar.

However, when the area fraction is increased, the decrease of the experimentally measured coefficient v^{pp} is much more pronounced than the decay seen for a hard-sphere monolayer. We ascribe this behavior to the presence of high-density regions in the strongly fluctuating drop system. In the dense regions, drops are displaced out of the midplane of the channel, as evidenced by the overlap of drop images seen in Fig. 7. The displaced drops generate increased friction with the walls, which hinders the emulsion flow and leads to the reduction of v^{pp} by about 30%.

The above observations help us provide an estimate for the convective transport coefficient χ_c in the high-area-fraction domains of the drop system, i.e., the regime for which experimental

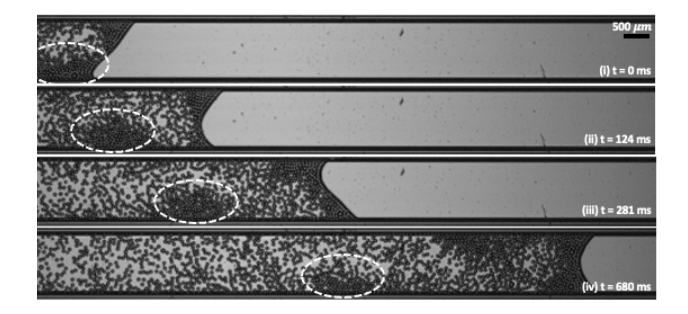


Fig. 9 Fingering instability and interface deformation during the imbibition of spherical droplets. Time-lapse images from an experiment with $\phi_a = 0.45$ at location 2, showing the fingering instability and deformation of the meniscus. The fingering instability results in separation of dense droplet clusters from the close-packed droplet band. The clusters (indicated by the white ellipses) migrate away from the meniscus and gradually disperse due to random droplet motions. Time t as labeled.

data are unavailable. The hard-sphere calculations show that χ_c is nearly independent of ϕ_a , as long as the particles remain in the midplane of the channel. However, the drops in high-density domains are shifted towards the channel walls during the imbibition process. Therefore, they reside in slower streamlines and their velocity is reduced. For a drop touching a wall, Faxen's law yields $\chi_c = 1.15$, which is lower than the value $\chi_c \approx 1.25$ for particles in the channel midplane. The particle-wall friction (not included in the Faxen's law value) further slows the drops down and reduces χ_c . However, even in the high density regime, χ_c always is larger than unity, as evidenced by the absence of a clear-fluid region behind the meniscus in the imbibition experiments.

In the following analysis of the effect of dense clusters on emulsion transport, we use $\chi_c = 1.25$ for low-concentration regions and $\chi_c = 1.1$ for dense clusters. These values are consistent with the particle-tracking measurements and the above estimates.

6.3 Suspension instability and interface deformation

Particle transport in the moderately confined system is much more complex than it would be in a macroscopically homogeneous emulsion monolayer. The complexity stems from flow instabilities in the dense droplet band near the meniscus (Fig. 9). The dense suspension is locally displaced by less dense and more mobile upstream suspension, which results in continuous generation of dense clusters intermixed with lower-density regions. The obPage 13 of 21 Soft Matter

served strong fluctuations of the area fraction and the existence of a systematic area-fraction gradient in the axial direction arise from this instability, as discussed below.

The observed emulsion flow instability is analogous to the Saffman–Taylor viscous fingering instability 70 in a Hele–Shaw cell. The driving pressure force produces stronger flow in the low-viscosity domains; thus the low-viscosity fluid penetrates into the high-viscosity regions, forming fingers. A similar behavior occurs in suspension imbibition, where regions with a lower areafraction have a larger permeability coefficient v^{pp} than the high area-fraction regions according to the data shown in Fig. 8. Thus, a given pressure gradient generates stronger flow, producing low-area-fraction fingers penetrating the high-density domain.

Hydrodynamic stresses associated with the motion of low-density fingers can result in meniscus deformation (Fig. 9). The deformation, in turn, facilitates finger formation because it breaks the hexagonally ordered suspension structure in the closely packed region near the suspension front. We do not expect, however, that the meniscus instability strongly affects the capillary pressure, because the observed interface deformation occurs in the direction along the channel width w, and the main capillary pressure contribution is produced by the much larger interface curvature across the channel height $h \ll w$.

Closely packed ordered emulsion has a nonzero yield stress, so development of an ordered structure may prevent finger formation, allowing a buildup of a large hexagonally ordered dense domain. This behavior is more pronounced at a stronger confinement (e.g., d/h = 0.8). Formation of hexagonal structures is also predicted by our numerical Hele–Shaw dipolar model (Fig. 10).

When a low-density finger approaches the meniscus, it usually turns toward a channel side wall. After touching the wall, the finger causes separation of a dense droplet cluster from the close-packed droplet band near the meniscus. As seen from the time-lapse images presented in Fig. 9, the separated clusters migrate backward relative to the meniscus. However, as shown in the following section, this backward migration does not require $\chi_c < 1$, because it results from different volumetric suspension velocities \bar{u} at different transverse positions in the channel.

After separation, the dense clusters gradually decay as a result of hydrodynamically induced random droplet displacements. Drop accumulation near the meniscus followed by cluster separation repeats in a quasi-periodic manner, causing the observed large area-fraction fluctuations and formation of a systematic area-fraction gradient seen in Fig 1(f).

6.4 An analysis of cluster migration

The cluster-migration mechanism (Fig. 11) in a moderately confined emulsion vastly differs from the dynamics of dense domains at strong confinement. For strongly confined disk-like drops, dense domains often span the entire channel width (Fig. 11(a)). By the continuity condition, the suspension velocity is the same behind, in, and in front of the domain, and the particle motion is controlled by the convective transport relation (6). Since the convective transport coefficient has the largest value in the dense region ($\chi_{c1}, \chi_{c3} < \chi_{c2}$ in the notation of Fig. 11(a)), particles in

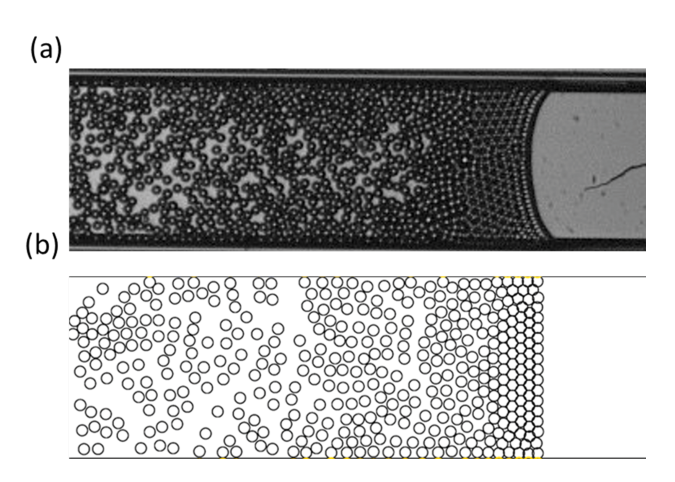


Fig. 10 Hele–Shaw dipolar model predicts formation of a hexagonally packed droplet band. A qualitative comparison between (*a*) the droplet band formed in an experiment with $\phi_a = 0.53$ at location 2 and (*b*) a droplet band predicted by the Hele-Shaw dipolar model. The meniscus is simulated using a repulsive force that acts opposite to the flow direction.

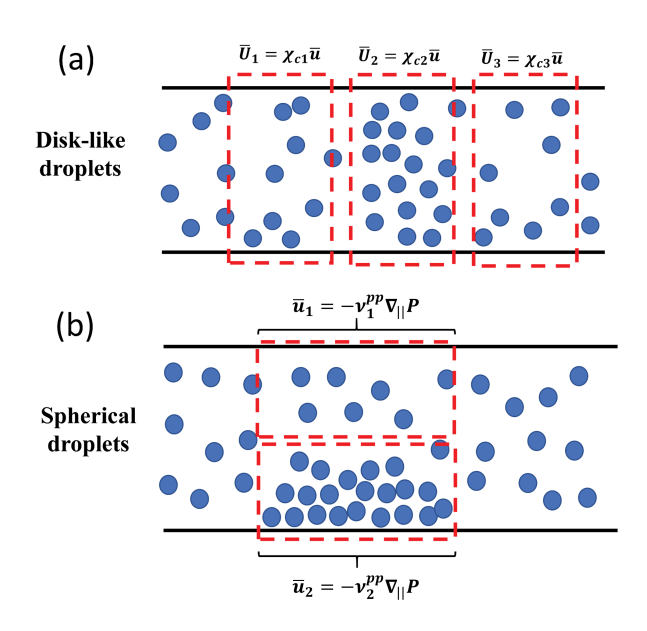


Fig. 11 A schematic representation of the dynamics of dense droplet clusters for disk-like and spherical droplet systems. (a) Dense clusters of disk-like droplets usually span the whole width of the channel and their dynamics is governed by the convective transport coefficient χ_c . Since χ_c is an increasing function of the area fraction, the drops in a dense region move faster than those in less dense regions behind and in front of it. (b) Dense clusters of spherical droplets do not span the whole width of the channel and their dynamics is governed by the permeability coefficient v^{pp} . Since v^{pp} decreases with the area fraction, a dense cluster moves slower than the adjacent less dense region.

the dense domain move faster than the ones in the lower areafraction zones, resulting in a forward-propagating density wave.

In contrast, in a system of spherical droplets, the clusters that separate from the dense droplet band do not span the entire channel width (Fig. 11(b)). Their motion and the motion of the neighboring low-density regions are governed by locally applied mobility relations (5). In particular, for the local volumetric suspension

Soft Matter Page 14 of 21

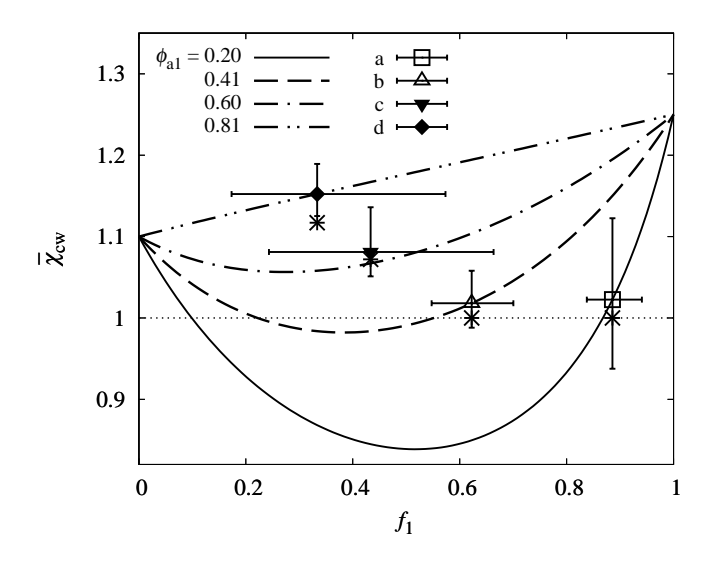


Fig. 12 Width-averaged effective convective transport coefficient $\bar{\chi}_{cw}$ in the presence of backward migrating close-packed clusters. The graph shows the width-averaged effective convective transport coefficient $\bar{\chi}_{cw}$ vs the fraction of the low-density domain f_1 , for four values of the area fraction of the dilute region ϕ_{a1} (as labeled). These values correspond to the four systems (a)–(d) depicted in Fig. 14. The lines represent the theoretical expression (46), and the diamond, triangles, and square describe $\bar{\chi}_{cw}$ calculated from the measured low-density and width-averaged area fractions ϕ_{a1} and $\bar{\phi}_{aw}$ for the four systems presented in Fig. 14 (see Appendix A for the measurement details). The low-density fraction f_1 is determined from ϕ_{a1} and $\bar{\phi}_{aw}$ using eqn (45), and $\bar{\chi}_{cw}$ is evaluated using eqn (46). The error bars reflect inaccuracies of the estimates of ϕ_{a1} and $\bar{\phi}_{aw}$. The open symbols represent systems for which the theory predicts self-adjustment of f_1 towards the value for which $\bar{\chi}_{cw} \approx 1$; the closed symbols represent systems with $\bar{\chi}_{cw} > 1$ for arbitrary values of f_1 . Consistent with our prediction, the systems (a) and (b) in Fig. 14 show no buildup of the close packed zone, and a buildup is observed in systems (c) and (d). The estimates for the convective transport coefficient $\bar{\chi}_{\scriptscriptstyle CW}$ that are based on the observed growth rate of the compact region in systems shown in Fig. 14(a)–(d) are indicated by the asterisks.

motion we have

$$\bar{u}_1 = -v_1^{pp} \nabla_{\parallel} p_1$$
 lower density region, (37a)

$$\bar{u}_2 = -v_2^{pp} \nabla_{\parallel} p_2$$
 dense cluster, (37b)

where the indices 1 and 2 refer to the low-density and densecluster domains. Since the pressure gradient in the cluster and in laterally adjacent low-density region is approximately the same,

$$\nabla_{\parallel} p_1 = \nabla_{\parallel} p_2, \tag{38}$$

we find that

$$\frac{\bar{u}_2}{\bar{u}_1} = \frac{v_2^{pp}}{v_1^{pp}}. (39)$$

In high-area-fraction clusters the drops are displaced toward the walls, and the permeability coefficient is low, $v_2^{pp} < v_1^{pp}$. Thus, consistent with the results shown in Fig. 8, clusters move slower than the emulsion in the adjacent dilute regions.

The meniscus velocity $dL/dt = \bar{u}_w$ equals the emulsion velocity averaged across the channel width w,

$$\bar{u}_w = f_1 \bar{u}_1 + f_2 \bar{u}_2, \tag{40}$$

where f_1 and $f_2 = 1 - f_1$ denote the fractions of the channel width occupied by the dilute suspension and the cluster, respectively. Assuming that the cluster velocity \bar{U}_C equals the particle-phase velocity in the dense region,

$$\bar{U}_C = \chi_{c2}\bar{u}_2,\tag{41}$$

and combining relations (39), (40), and (41), we obtain

$$\frac{\bar{U}_C}{\bar{u}_w} = \frac{\chi_{c2}\varepsilon}{f_1 + f_2\varepsilon},\tag{42}$$

where

$$\varepsilon = V_2^{pp} / V_1^{pp} \tag{43}$$

is the permeability-coefficient ratio between the high-density and low-density regions. For a sufficiently small ratio (43) and the convective transport coefficient χ_{c2} close to unity, we have $\bar{U}_C/\bar{u}_w < 1$, according to eqn (42). Thus, clusters migrate away from the meniscus, consistent with the behavior seen in Fig. 9.

The time-lapse images of cluster separation in Fig. 9 yield $\bar{U}_C/\bar{u}_w = 0.6$ and $f_1 = 0.57$. Taking the approximate values $\chi_{c1} =$ 1.25 and $\chi_{c2} = 1.1$ for the convective transport coefficients, we obtain $v_2^{pp}/v_1^{pp} = 0.40$, according to equations (39)–(43). The above estimate for $\varepsilon = v_2^{pp}/v_1^{pp}$, consistent with our measurements (Fig. 8), is used in the cluster-transport analysis (Figs. 12-14).

The effective convective transport coefficient

The backward transport of dense particle clusters relative to the suspension volumetric flow reduces the effective convective transport coefficient $\bar{\chi}_{cw}$ that describes particulate-phase flow averaged across the entire channel width. As shown below, such reduction slows down or even prevents the buildup of the higharea-fraction band near the meniscus and results in generation of a systematic area-fraction gradient that is sustained during the course of an imbibition experiment.

To quantify this behavior, we use the two-zone suspension transport model described by eqns (37)-(43). The channelwidth-averaged effective convective transport coefficient $\bar{\chi}_{cw}$ is determined from the particle-phase flux balance

$$\bar{\phi}_{aw}\bar{\chi}_{cw}\bar{u}_w = f_1\phi_{a1}\chi_{c1}\bar{u}_1 + f_2\phi_{a2}\chi_{c2}\bar{u}_2. \tag{44}$$

Here ϕ_{a1} and ϕ_{a2} are the area fractions in the dilute regions and in the clusters, respectively, and

$$\bar{\phi}_{aw} = f_1 \phi_{a1} + f_2 \phi_{a2} \tag{45}$$

is the area fraction averaged across the width of the channel. The average emulsion velocity \bar{u}_w is defined by eqn (40). Combining eqn (44) with eqns (39), (40), and (43), we get

$$\bar{\chi}_{CW} = \frac{f_1 \phi_{a1} \chi_{c1} + f_2 \phi_{a2} \chi_{c2} \varepsilon}{\bar{\phi}_{aW} (f_1 + f_2 \varepsilon)}.$$
 (46)

The result (46) is plotted in Fig. 12 vs the width fraction f_1 of the dilute domain for different values of the area fraction ϕ_{a1} in this region. For small and moderate values of ϕ_{a1} , the coefficient $\bar{\chi}_{cw}$ has a minimum, with a value $\bar{\chi}_{cw}^{min} < \chi_{c1}, \chi_{c2}$. The reduction Page 15 of 21 Soft Matter

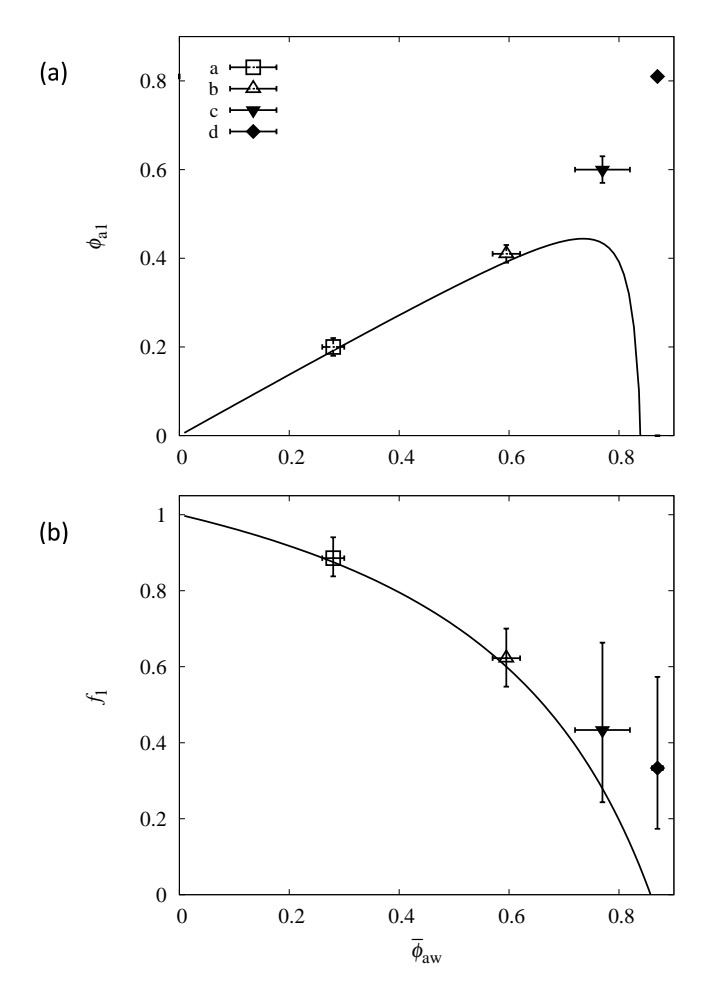


Fig. 13 System parameters required by the stationary particle-phase flux condition $\bar{\chi}_{cw}=1$. Solid lines describe the stationary flux conditions (47) for (a) the area fraction ϕ_{a1} and (b) width fraction f_1 of the low density region shown vs the width-averaged area fraction $\bar{\phi}_{aw}$. The symbols represent $\bar{\phi}_{aw}$ and ϕ_{a1} and the corresponding values of f_1 for the experimental systems depicted in Fig. 14(a)–(d). Since $\bar{\chi}_{cw}=1$ can be obtained only for $\phi_{a1}\lesssim 0.45$ according to the results in the top panel, the theory predicts that for downstream area fractions above this threshold value there is a buildup of the close-packed region behind the meniscus. The experimental results are consistent with this prediction.

of the effective convection transport coefficient χ_c relative to the values in the clusters and in the low-density regions stems from the fact that the faster volumetric flow in a low-density domain carries fewer particles per unit area than the slower flow that convects high-density clusters. Since the velocity in a cluster is lower than the width-averaged suspension velocity, on average the particles move slower than they would at a uniform density.

Moreover, for sufficiently low ϕ_{a1} , the effective convective transport coefficient $\bar{\chi}_{cw}$ can be smaller than unity, in spite of the fact that $\chi_{c1}, \chi_{c2} > 1$. The regime $\bar{\chi}_{cw} < 1$, i.e., that of particle-phase transport rate below the emulsion flow rate, occurs in the mid-range interval $f_1^- \leq f_1 \leq f_1^+$ of the width fractions f_1 , where f_1^\pm are the lower and upper limiting values.

6.6 The flux-balance condition

While, in principle, the domain $\bar{\chi}_{cw} < 1$ can be obtained by imposing an appropriate cluster distribution in the channel, this regime cannot be spontaneously achieved in an imbibing emulsion because the drop phase would move slower than the meniscus. There would be no densely packed zone near the imbibition front in this case, and dense clusters, which are essential for reducing the effective convective transport coefficient $\bar{\chi}_{cw}$, would not be generated. As a result, the fraction $f_2 = 1 - f_1$ of the channel width occupied by the clusters would decrease. Correspondingly, the low-density fraction f_1 would increase towards the threshold value $f_1 = f_1^+$, at which point the dynamical balance $\bar{\chi}_{cw} \approx 1$ between incoming particles and outgoing clusters would be established. Our model thus predicts that the system self-adjusts toward the flux-balance conditions.

According to eqns (45) and (46), the dynamic flux balance $\bar{\chi}_{cw} = 1$ is achieved for ϕ_{a1} and f_1 given by the expressions

$$\frac{\phi_{a1}}{\bar{\phi}_{aw}} = \frac{\phi_{a2}(1 - \chi_{c2}\varepsilon) - \bar{\phi}_{aw}(1 - \varepsilon)}{\phi_{a2}(\chi_{c1} - \chi_{c2}\varepsilon) + \bar{\phi}_{aw}(1 - \varepsilon)}$$
(47a)

and

$$f_{1} = \frac{\phi_{a2}(\chi_{c1} - \chi_{c2}\varepsilon) + \bar{\phi}_{aw}(1 - \varepsilon)}{\phi_{a2}(\chi_{c1} - \chi_{c2}\varepsilon) - \bar{\phi}_{aw}(1 - \varepsilon)}.$$
 (47b)

The area fraction ϕ_{a1} and channel-width fraction f_1 determined from eqns (47) are plotted in Fig. 13.

6.7 Area fraction threshold for the formation of a closely packed emulsion band behind the meniscus

An important feature of the curve shown in Fig. 13(a) is that the function (47a), describing the flux-balance value of ϕ_{a1} , has a maximum $\phi_{a1} = \phi_a^{\rm crit}$, at $\bar{\phi}_{aw} = 0.734$, with $\phi_a^{\rm crit} = 0.444$. This behavior, consistent with the results depicted in Fig. 12, indicates that the dynamic flux-balance condition cannot be established for $\phi_{a1} > \phi_a^{\rm crit}$. Hence, for $\phi_{a1} > \phi_a^{\rm crit}$, we have $\bar{\chi}_{cw} > 1$ for all values of f_1 , and, on average, the particles move faster than the meniscus, leading to a continuous growth of a dense domain near the imbibition front. In contrast, for $\phi_{a1} < \phi_a^{\rm crit}$, a self-adjustment of the system toward the flux-balance condition $\bar{\chi}_{cw} \approx 1$ occurs.

Recalling that the emulsion microstructure that involves dense clusters and low-area-fraction regions is generated by the fingering instability (Fig. 9), we can assume that the local area fraction ϕ_{a1} equals the upstream area fraction of the suspension invading the concentrated domain. Thus we expect that for upstream area fractions that are smaller than the critical value $\phi_a^{\rm crit}$, the growth of a dense layer near the imbibition front is arrested, and above the critical value, the growth can be slowed down but cannot be eliminated by the fingering instability.

The predicted self-adjustment of $\bar{\chi}_{cw}$ toward unity at low upstream area fractions and the transition to the buildup of a dense domain at higher area fractions are observed in our experiments. This behavior is illustrated in Fig. 14, where we compare imbibition results for four area fractions ϕ_{a1} . As described in Appendix A, the area fraction ϕ_{a1} is estimated based on the measurements in an upstream region near the point where the backward migrating clusters have already significantly dispersed. The area fraction

Page 16 of 21

Soft Matter

 $\bar{\phi}_{aw}$ is evaluated in the region closer to the meniscus, where dense clusters and low-density regions coexist.

At the lowest area fraction $\phi_{a1} \approx 0.2$ (Fig. 14(*a*)), dense clusters are small and far apart, corresponding to the large width fractions, $f_1 \lesssim 1$, and small $\bar{\phi}_{aw}$ in Fig. 13. At a higher upstream area fraction $\phi_{a1} \approx 0.4$ (Fig. 14(b)) the clusters form more frequently and are larger, but in both cases the dynamical equilibrium is maintained between the incoming particle flux and particles removed from the region near meniscus by the fingering instability.

For sufficiently large area fractions, the close-packed droplet layer behind the meniscus continuously expands (Fig. 14(c) and (d)), consistent with our predictions. The rate of this expansion increases with the upstream drop area fraction, and the width fraction f_1 occupied by the lower-density domains decreases.

6.8 A quantitative comparison of theoretical predictions with experiments

The area fraction measurements for the systems shown in Fig. 14 allow us to perform a semiquantitative comparison of the experimental results with our theoretical predictions. To this end, the measured values of ϕ_{a1} and $\bar{\phi}_{aw}$ are inserted into eqns (45) and (46) to evaluate the width fractions f_1 and f_2 and determine the effective convective transport coefficient $\bar{\chi}_{cw}$ in the cluster migration zone behind the meniscus.

The results are shown in Figs. 12 and 13. The open symbols correspond to the low-density systems below the dense-regionbuildup threshold $\phi_a^{\mathrm{crit}}.$ The calculated values of $\bar{\chi}_{\scriptscriptstyle CW}$ are close to the predicted value $\bar{\chi}_{cw}=1$, and the fraction of the lowconcentration domains is close to $f_1 \approx f_1^+$ (Fig. 12). The experimental points are also very close to the theoretical lines $\bar{\chi}_{cw} = 1$ shown in Fig. 13. The closed symbols describe conditions where the area fraction is above the dense-region-buildup threshold. For the measured values of ϕ_{a1} and $\bar{\phi}_{aw}$, we get $\bar{\chi}_{cw} > 1$ (Fig. 12). Moreover, in Fig. 13 these experimental points are significantly above the lines describing the flux balance condition $\bar{\chi}_{cw} = 1$, consistent with the predicted behavior.

The calculated values of $\bar{\chi}_{cw}$ for the above-critical systems (c) and (d) can be used to estimate the growth rate of the dense layer behind the meniscus

$$\frac{\dot{L}_{\rm cp}}{\bar{u}_w} = \frac{\bar{\phi}_{aw}(\bar{\chi}_{cw} - 1)}{\phi_{a\rm CP}},\tag{48}$$

where the $L_{\rm cp}$ is the size of the close-packed layer, the dot denotes the time derivative, \bar{u}_w is the width-averaged emulsion velocity (equal to the meniscus velocity), and $\phi_{aCP} \approx 0.9$ is the closepacking area fraction in the compact region. For the systems (c) and (d), relation (48) with the values of $\bar{\phi}_{aw}$ and $\bar{\chi}_{cw}$ presented in Figs. 12 and 13 yields $\dot{L}_{\rm cp}/\bar{u}_{\rm w}=0.068$ and 0.15, respectively. The direct measurements based on images depicted in Fig. 14(c) and (d) yield $\dot{L}_{\rm cp}/\bar{u}_{\rm w}=0.062$ and 0.12, which agrees with the theoretical estimates within 20%. Conversely, eqn (48) can be used to determine $\bar{\chi}_{cw}$ from the measured values of \dot{L}_{cp} ; the results of this estimate are marked with the asterisks in Fig. 12.

To sum up, our theoretical analysis presents the key qualitative features of moderately confined imbibition system and provides semiquantitative theoretical predictions for its dynamics. Taking into account (i) large inaccuracies of the area-fraction measurements in an emulsion with strongly fluctuating concentration, (ii) lack of borders between close-packed, cluster-migration, and uniform upstream regions, and (iii) significant simplifications underlying our theoretical calculations, the agreement between the theoretical and experimental results is very good.

6.9 Formation of a systematic drop concentration gradient

The local area-fraction measurements (Figs. 1 and A.1) show that, in addition to strong density fluctuations, there exists a systematic area-fraction gradient pointing downstream. Our analysis of the imbibition dynamics (Secs. 6.2–6.8) allows us to identify the main mechanisms of the density-gradient generation and to make conclusions regarding long-time system evolution.

Essential phenomena contributing to the formation and time evolution of the density gradient include (i) the overall particlephase transport toward the meniscus; (ii) generation of strong density fluctuations by a fingering instability; (iii) reduction of the particle transport rate in a region of strong density fluctuations; and (iv) decay of density fluctuations due to hydrodynamic diffusion, resulting in decomposition of dense clusters.

We propose that the imbibition system evolves as follows: Since for any area fraction we have $\chi_c > 1$ near the capillary entrance where no dense clusters are present, the overall upstream dropphase velocity is larger than the meniscus velocity. Thus, the drop density behind the meniscus gradually increases. Initially, the drops collect next to the meniscus in a close-packed layer, but for upstream area fractions that are below the critical value ϕ_a^{crit} , the growth of the dense layer is temporarily arrested by the mechanism associated with the fingering instability (Secs. 6.6 and 6.7). Such arrest is observed for systems (a) and (b) shown in Fig. 14.

The arrest of growth of the close-packed layer is transient because clusters decay due to hydrodynamic diffusion. Thus, the clusters can transport particles back only over a finite distance. The cluster dissolution, evident in the time-lapse images (Fig. 9), results in an increase of the area fraction in the suspension domain at the upstream edge of the inhomogeneous domain generated by the fingering. As a result, the area fraction of the suspension that enters the fingers between the high-density domains gradually increases. When it reaches the critical value ϕ_a^{crit} , a gradual buildup of the close-packed layer behind the meniscus commences. The long-time growth rate of the close-packed layer can be evaluated from the relation analogous to eqn (48) but with the values of the area fraction and convective transport coefficients determined at the capillary entrance rather than in the fluctuating domain generated by the fingering instability.

Based on our results for the convective transport coefficient χ_c and the area fraction ϕ_a^{crit} , we estimate that for the area fraction at the capillary entrance $\phi_a \approx 0.35$, the transition from a stationary to growing compact layer near the meniscus would occur when the meniscus is approximately 4 cm from the entrance, which is outside our experimental observation window. For lower entrance area fractions the transition would occur even later. We expect that at long times the system achieves a steady-state density disPage 17 of 21 Soft Matter

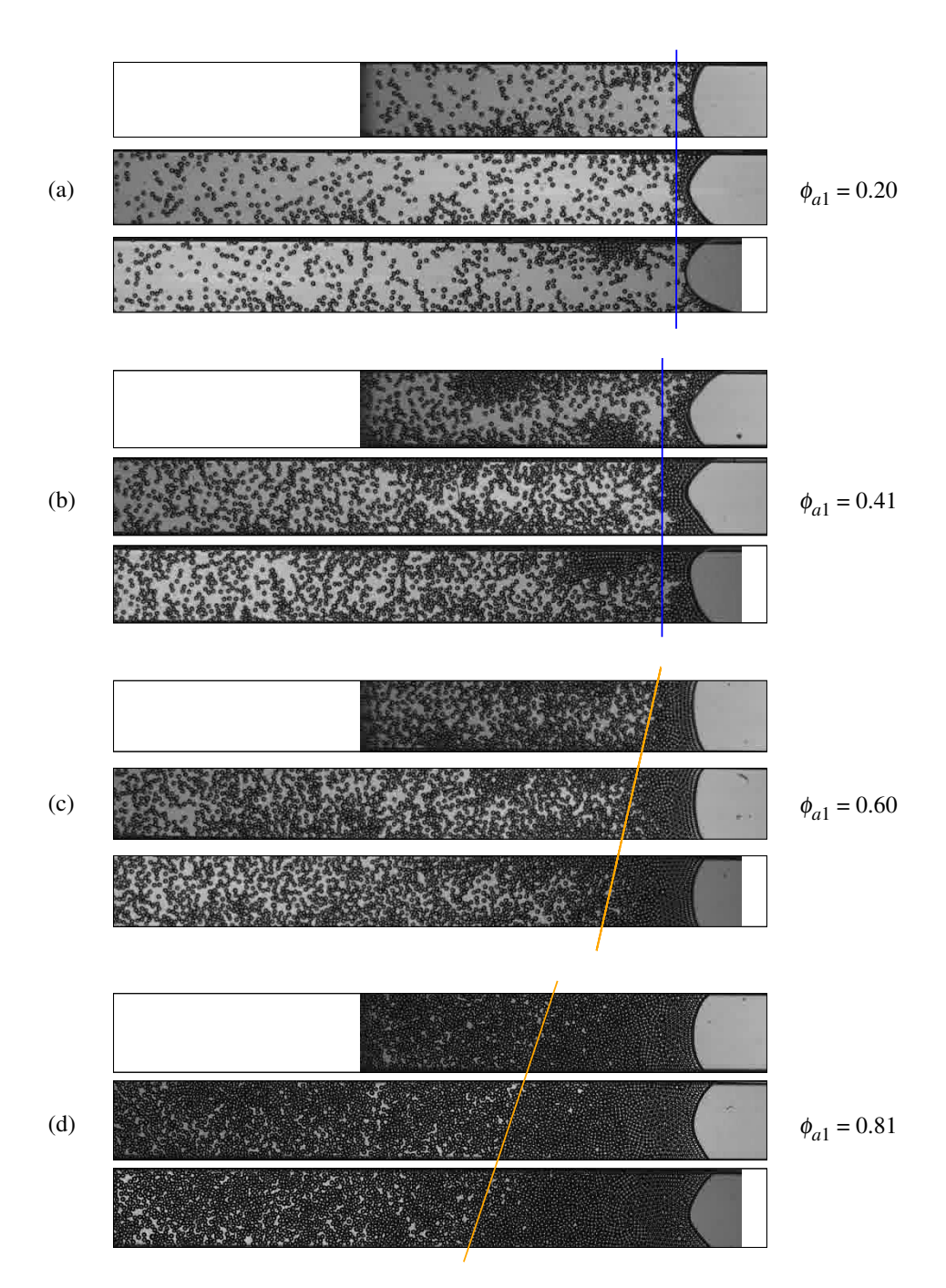


Fig. 14 Evolution of a high-density band for systems with different upstream area fractions. (a)–(d) Time-lapse images of emulsions of moderately confined drops (d/h = 0.65) showing the evolution of the high-density band behind the meniscus for different area fractions ϕ_{a1} (as labeled) measured at the downstream edge of the cluster-migration region. The images are aligned on the meniscus. The position of the meniscus in the top, middle and bottom panels for each area fraction is x = 18.3 mm, 21.4 mm, and 23.5 mm, respectively. At the lower values of ϕ_{a1} the width of the dense band does not grow in time (blue lines), whereas at the higher upstream area fractions the size of the dense band increases (orange lines).

tribution relative to the upstream border of the dense-packed region. The density profile in this steady state is determined by the mixing mechanism associated with generation, migration, and decay of dense clusters and can be analyzed using the ideas presented above. A more detailed investigation of this problem, however, is beyond the scope of the present study.

7 Conclusions

The presented results demonstrate rich phenomenology of the emulsion imbibition under strong and moderate confinement conditions (i.e., when the drop diameter is either somewhat larger or somewhat smaller than the channel height). We have shown that the imbibition dynamics and drop distribution are strongly influenced by the degree of confinement, with striking differences between the strong and moderate confinement cases.

Soft Matter Page 18 of 21

For strong confinements, i.e., when droplets squeezed between two channel walls deform to a disk-like shape, we observe formation of a droplet-free region behind the meniscus, separated from the suspension region by a sharp density front. Droplets in the suspension region show large velocity and area fraction fluctuations and density-wave propagation.

For moderately confined spherical droplets, a dense droplet band forms behind the meniscus. The band undergoes fingering instability, and, depending on the upstream drop area fraction, the band width is either constant or grows. In addition, a gradual density variation occurs along the length of the channel.

We show that many aspects of the above rich phenomenology can be described using coarse-grained suspension transport equations that involve two independent constitutive relations. These relations link the volumetric suspension velocity and particlephase velocity to the applied pressure gradient. Combining these two equations, we obtain the convective-transport equation that relates the particle-phase and suspension velocities.

Since we have also measured the corresponding three constitutive transport coefficients (the permeability coefficient v^{pp} , particle-phase mobility v^{tp} , and convective transport coefficient χ_c), the constitutive relations and measured transport coefficients have helped elucidate the major differences between the dynamics of highly confined and moderately confined emulsions. Our theory captures important aspects, such as the formation of a sharp front between the suspension and clear fluid for highly confined drops and the existence of a critical area fraction for the buildup of a close-packed region in moderately confined systems. Microscale details, such as the role of transient drop chains, have been explained using a dipolar-interaction simulation model.

While our experiments were performed only for several confinements ratios, our theoretical approach makes it possible to predict the dynamics of emulsion imbibition also at other confinements. Depending on specific applications, our results may help determine conditions where imbibition distributes particles uniformly throughout the channel or brings them close to the imbibition front. Our predictions of velocity fluctuations that are caused by drop chain and cluster dynamics may impact design of novel systems for efficient mixing in microfluidic channels.

We note that the constitutive equations used here are a part of a larger set of constitutive relations that link the suspension and particle velocities to two driving forces: the pressure gradient $\nabla_{\parallel} p_s$ and force applied to the particles. Due to Onsager/Lorentz symmetry for particles undeformed by the flow, the transport coefficient v^{tp} is directly related to the coefficient v^{pt} that describes the suspension velocity \bar{u} generated by the force applied to the particles. 57 Since, apart from drop flattening in the strongly confined case, drops in our system do not undergo flow-induced deformation, our measurements of v^{tp} provide additional information regarding the emulsion response to a force acting on the particle phase. Thus, the implications of our study extend beyond the imbibition process.

Author contributions

MND: experimental investigation, validation, visualization, writing-original draft. SS: simulation software development,

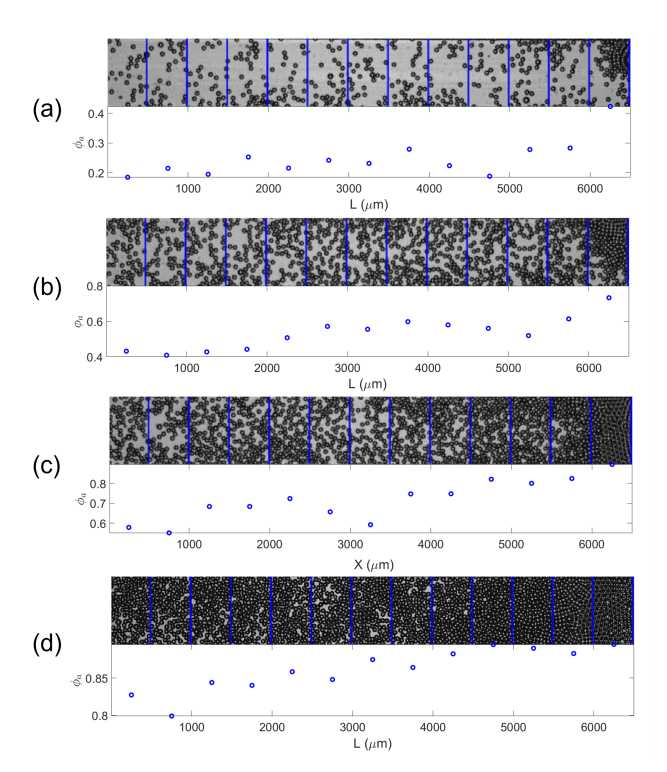


Fig. A.1 Area fraction distribution for the four systems depicted in Fig. 14. The plots below each image show the area fraction of droplets in small subregions within the field of view once the meniscus has reached the end of the field.

numerical investigation, visualization. SAV: conceptualization, methodology, supervision, resources. MWV: conceptualization, methodology, supervision, resources, funding acquisition, project administration, writing-editing. JB: conceptualization, formal analysis, supervision, validation, writing-original draft, reviewing and editing. All authors reviewed the final draft.

Conflict of interest

There are no conflicts to declare.

Acknowledgements

Acknowledgement is made to the donors of the American Chemical Society Petroleum Research Fund grant #59482-ND5 for support of MWV and MND in this research. SS and JB were supported by NSF Grant CBET 1603627. We thank Purushottam Soni for the surface tension measurement.

Appendix A

Figure A.1 shows the area fraction profile along the channel for the four systems depicted in Fig. 14. In all cases the area fraction strongly fluctuates and exhibits a systematic increase in the downstream direction (toward the meniscus).

The area fraction ϕ_{a1} is estimated from the local area fraction in the region close to the upstream border of the cluster-migration zone generated by the fingering instability. The lower-density emulsion from this region enters the upstream high-density domain, forming fingers. Thus, the measured downstream area fraction can be identified with the area fraction ϕ_{a1} in our theory. The Page 19 of 21 Soft Matter

Table A.1 Values of the area fractions ϕ_{a1} and $\bar{\phi}_{aw}$ used in the calculations presented in Figs. 12 and 13.

System	ϕ_{a1}	$ar{\phi}_{aw}$
(a)	0.20 ± 0.02	0.28 ± 0.02
(b)	0.41 ± 0.02	0.595 ± 0.025
(c)	0.60 ± 0.03	0.77 ± 0.05
(d)	0.81 ± 0.02	0.87 ± 0.01

width-averaged area fraction $\bar{\phi}_{aw}$ is determined from the measurements closer to the meniscus in the domain where coexisting low-density fingers and dense clusters are present.

In Fig. A.1 the upstream edge of the cluster-migration zone is near the left border of the presented images, i.e., close to the region where most of the backward-migrating clusters have already decayed; ϕ_{a1} is estimated based on the area fraction in this domain. The values of $\bar{\phi}_{aw}$ are obtained from the area fraction measured close to the edge of the densely packed region.

The estimated values of ϕ_{a1} and $\bar{\phi}_{aw}$ (Table A.1) are used in our theoretical analysis presented in Figs. 12 and 13. Since there is no sharp transition between the cluster-migration zone and the upstream emulsion that enters the high-density downstream region, the data in Table A.1 should be treated as semi-quantitative estimates rather than precisely measured values.

References

- 1 G. Libri, Histoire des sciences mathématiques en Italie: depuis la renaissance des lettres jusqu'à la fin du dix-septieme siècle, HW Schmidt, 1865, vol. 2.
- 2 E. Macagno, Some remarkable experiments of Leonardo da Vinci, *La Houille Blanche*, 1991, 77, 463–471.
- 3 E. W. Washburn, The dynamics of capillary flow, *Physical Review*, 1921, **17**, 273.
- 4 D. Quéré, Inertial capillarity, EPL (Europhysics Letters), 1997, 39, 533.
- 5 N. Fries and M. Dreyer, The transition from inertial to viscous flow in capillary rise, *Journal of Colloid and Interface Science*, 2008, **327**, 125–128.
- 6 M. Bracke, F. De Voeght and P. Joos, The kinetics of wetting: the dynamic contact angle, *Trends in Colloid and Interface Science III*, 1989, 142–149.
- 7 A. Siebold, M. Nardin, J. Schultz, A. Walliser and M. Oppliger, Effect of dynamic contact angle on capillary rise phenomena, Colloids and Surfaces A: Physicochemical and Engineering Aspects, 2000, 161, 81–87.
- 8 M. N. Popescu, J. Ralston and R. Sedev, Capillary rise with velocity-dependent dynamic contact angle, *Langmuir*, 2008, **24**, 12710–12716.
- 9 A. Budaraju, J. Phirani, S. Kondaraju and S. S. Bahga, Capillary Displacement of Viscous Liquids in Geometries with Axial Variations, *Langmuir*, 2016, **32**, 10513–10521.
- 10 S. Khatoon, J. Phirani and S. S. Bahga, An analytical solution of the inverse problem of capillary imbibition, *Phys. Fluids*, 2020, **32**, 041704.
- 11 S. Ashraf, Y. Méheust and J. Phirani, Spontaneous imbibi-

- tion dynamics in two-dimensional porous media: A generalized interacting multi-capillary model, *Phys. Fluids*, 2023, **35**, 012005.
- 12 E. Delamarche, A. Bernard, H. Schmid, B. Michel and H. Biebuyck, Patterned delivery of immunoglobulins to surfaces using microfluidic networks, *Science*, 1997, 276, 779–781.
- 13 O. Gökçe, S. Castonguay, Y. Temiz, T. Gervais and E. Delamarche, Self-coalescing flows in microfluidics for pulse-shaped delivery of reagents, *Nature*, 2019, **574**, 228–232.
- 14 N. Morrow and G. Mason, Recovery of oil by spontaneous imbibition, *Current Opinion in Colloid & Interface Science*, 2001, 6, 321–337.
- 15 A. Clarke, T. Blake, K. Carruthers and A. Woodward, Spreading and imbibition of liquid droplets on porous surfaces, *Langmuir*, 2002, 18, 2980–2984.
- 16 R. Zhou and H.-C. Chang, Capillary penetration failure of blood suspensions, *Journal of Colloid and Interface Science*, 2005, **287**, 647–656.
- 17 S. Chakraborty, Dynamics of capillary flow of blood into a microfluidic channel, *Lab on a Chip*, 2005, **5**, 421–430.
- 18 C. L. Berli and R. Urteaga, Asymmetric capillary filling of non-Newtonian power law fluids, *Microfluidics and Nanofluidics*, 2014, 17, 1079–1084.
- 19 Y. Yao, S. Alexandris, F. Henrich, G. Auernhammer, M. Steinhart, H. Butt and G. Floudas, Complex dynamics of capillary imbibition of poly (ethylene oxide) melts in nanoporous alumina, *The Journal of Chemical Physics*, 2017, 146, 203320.
- 20 J. D. Beard, D. Rouholamin, B. L. Farmer, K. E. Evans and O. R. Ghita, Control and modelling of capillary flow of epoxy resin in aligned carbon nanotube forests, *RSC Advances*, 2015, 5, 39433–39441.
- 21 D. Psaltis, S. R. Quake and C. Yang, Developing optofluidic technology through the fusion of microfluidics and optics, *Nature*, 2006, **442**, 381–386.
- 22 J. Dhar, P. Jaggi and S. Chakraborty, Oscillatory regimes of capillary imbibition of viscoelastic fluids through concentric annulus, *RSC Advances*, 2016, **6**, 60117–60125.
- 23 U. R. Sumanasekara, M. N. Azese and S. Bhattacharya, Transient penetration of a viscoelastic fluid in a narrow capillary channel, *Journal of Fluid Mechanics*, 2017, **830**, 528–552.
- 24 D. Shou and J. Fan, The fastest capillary penetration of power-law fluids, *Chemical Engineering Science*, 2015, **137**, 583–589.
- 25 J. Siddique and D. Anderson, Capillary rise of a non-Newtonian liquid into a deformable porous material, *Journal of Porous Media*, 2011, **14**, 1087–1102.
- 26 N. Srivastava and M. A. Burns, Analysis of non-Newtonian liquids using a microfluidic capillary viscometer, *Analytical Chemistry*, 2006, **78**, 1690–1696.
- 27 M. A. I. Rashid, S. Ansari, P. R. Waghmare and D. Nobes, Capillary filling of Non-Newtonian fluids, 10th Pacific Symposium on Flow Visualization and Image Processing, 2015, Paper ID:132.
- 28 W. Holloway, J. M. Aristoff and H. A. Stone, Imbibition of con-

Soft Matter Page 20 of 21

- centrated suspensions in capillaries, Physics of Fluids, 2011, **23**, 081701.
- 29 H. Tang, W. Grivas, D. Homentcovschi, J. Geer and T. Singler, Stability considerations associated with the meniscoid particle band at advancing interfaces in Hele-Shaw suspension flows, Phys. Rev. Lett., 2000, 85, 2112.
- 30 J. Kim, F. Xu and S. Lee, Formation and destabilization of the particle band on the fluid-fluid interface, Physical Review Letters, 2017, 118, 074501.
- 31 S. Abedi, C. C. Chen and S. A. Vanapalli, Catastrophic thermal destabilization of two-dimensional close-packed emulsions due to synchronous coalescence initiation, Soft Matter, 2020, 16, 6032–6037.
- 32 S. Abedi, C. C. Chen and S. A. Vanapalli, Collective nucleation dynamics in two-dimensional emulsions with hexagonal packing, Physical Review E, 2020, 101, 030602.
- 33 M. Baron, J. Blawzdziewicz and E. Wajnryb, Hydrodynamic crystals: collective dynamics of regular arrays of spherical particles in a parallel-wall channel, Phys. Rev. Lett., 2008, **100**, 174502.
- 34 T. Beatus, T. Tlusty and R. Bar-Ziv, Burgers Shock Waves and Sound in a 2D Microfluidic Droplets Ensemble, Phys. Rev. Lett., 2009, 103, 114502.
- 35 T. Beatus, R. H. Bar-Ziv and T. Tlusty, The physics of 2D microfluidic droplet ensembles, Physics Reports, 2012, 516, 103-
- 36 T. Beatus, T. Tlusty and R. Bar-Ziv, Phonons in a onedimensional microfluidic crystal, Nature Phys., 2006, 2, 743-748.
- 37 S. Singha, A. R. Malipeddi, M. Zurita-Gotor, K. Sarkar, K. Shen, M. Loewenberg, K. B. Migler and J. Blawzdziewicz, Mechanisms of spontaneous chain formation and subsequent microstructural evolution in shear-driven strongly confined drop monolayers, Soft Matter, 2019, 15, 4873-4889.
- 38 M. Hashimoto, P. Garstecki, H. Stone and G. Whitesides, Interfacial instabilities in a microfluidic Hele-Shaw cell, Soft Matter, 2008, 4, 1403-1413.
- 39 P. Saffman, The lift on a small sphere in a slow shear flow, J. Fluid Mech., 1965, 22, 385.
- 40 B. Cui, H. Diamant, B. Lin and S. A. Rice, Anomalous hydrodynamic interaction in a quasi-two-dimensional suspension, Phys. Rev. Lett., 2004, 92, 258301-1-4.
- 41 S. Bhattacharya, J. Blawzdziewicz and E. Wajnryb, Manyparticle hydrodynamic interactions in parallel-wall geometry: Cartesian-representation method, Physica A, 2005, 356, 294-
- 42 S. Bhattacharya, J. Blawzdziewicz and E. Wajnryb, Hydrodynamic interactions of spherical particles in suspensions confined between two planar walls, J. Fluid Mech., 2005, 541, 263-292.
- 43 P. J. A. Janssen, M. D. Baron, P. D. Anderson, J. Blawzdziewicz, M. Loewenberg and E. Wajnryb, Collective dynamics of confined rigid spheres and deformable drops, Soft Matter, 2012, 8, 7495-7506.
- 44 J. Blawzdziewicz and E. Wajnryb, Phase equilibria in strat-

- ified thin liquid films stabilized by colloidal particles, Europhys. Lett., 2005, 71, 269-275.
- 45 A. Ramachandran and D. T. Leighton, The effect of gravity on the meniscus accumulation phenomenon in a tube, Journal of Rheology, 2007, 51, 1073-1098.
- 46 S. Anna, N. Bontoux and H. Stone, Formation of dispersions using "flow focusing" in microchannels, Appl. Phys. Lett., 2003, **82**, 364–366.
- 47 R. Dreyfus, P. Tabeling and H. Willaime, Ordered and Disordered Patterns in Two-Phase Flows in Microchannels, Phys. Rev. Lett., 2003, 90, 144505.
- 48 S. Abedi, N. S. Suteria, C.-C. Chen and S. A. Vanapalli, Microfluidic production of size-tunable hexadecane-in-water emulsions: Effect of droplet size on destabilization of twodimensional emulsions due to partial coalescence, Journal of Colloid and Interface Science, 2019, 533, 59-70.
- 49 Y. Xia and G. M. Whitesides, Soft Lithography, Annual Review of Materials Science, 1998, 28, 153-184.
- 50 E. Fuguet, C. Ràfols, M. Rosés and E. Bosch, Critical micelle concentration of surfactants in aqueous buffered and unbuffered systems, Analytica Chimica Acta, 2005, 548, 95-100.
- 51 H. Goldsmith and S. Mason, Axial Migration Of Particles In Poiseuille Flow, Nature, 1961, 190, 1095.
- 52 J. R. Smart and D. T. Leighton, Measurement of the drift of a droplet due to the presence of a plane, Phys. Fluids A, 1991, **3**, 21–28.
- 53 R. E. Kalman, A New Approach to Linear Filtering and Prediction Problems, Journal of Basic Engineering, 1960, 82, 35-45.
- 54 H. W. Kuhn, The Hungarian method for the assignment problem, Naval Research Logistics Quarterly, 1955, 2, 83–97.
- 55 E. Vignati, R. Piazza and T. Lockhart, Pickering emulsions: Interfacial tension, colloidal layer morphology, and trappedparticle motion, Langmuir, 2003, 19, 6650-6656.
- 56 S. Bhattacharya, J. Blawzdziewicz and E. Wajnryb, Far-field approximation for hydrodynamic interactions in parallel-wall geometry, J. Comput. Phys., 2006, 212, 718-738.
- 57 J. Blawzdziewicz and E. Wajnryb, An analysis of the far-field response to external forcing of a suspension in Stokes flow in a parallel-wall channel, Phys. Fluids., 2008, 20, 093303.
- 58 J. Blawzdziewicz and E. Wajnryb, Equilibrium and nonequilibrium thermodynamics of particle-stabilized thin liquid films, J. Chem. Phys., 2008, 129, 194509.
- 59 T. Beatus, T. Tlusty and R. Bar-Ziv, Anomalous microfluidic phonons induced by the interplay of hydrodynamic screening and incompressibility, Phys. Rev. Lett., 2007, 99, 124502.
- 60 L. Zhu and F. Gallaire, A pancake droplet translating in a Hele-Shaw cell: lubrication film and flow field, J. Fluid Mech., 2016, 798, 955-969.
- 61 L. Keiser, K. Jaafar, J. Bico and E. Reyssat, Dynamics of nonwetting drops confined in a Hele-Shaw cell, J. Fluid Mech., 2018, **845**, 245–262.
- 62 B. Reichert, I. Cantat and M.-C. Jullien, Predicting droplet velocity in a Hele-Shaw cell, Phys. Rev. Fluids, 2019, 4, 113602.
- 63 A. Huerre, O. Theodoly, A. M. Leshansky, M.-P. Valignat,

Page 21 of 21 Soft Matter

I. Cantat and M.-C. Jullien, Droplets in Microchannels: Dynamical Properties of the Lubrication Film, *Phys. Rev. Lett.*, 2015, **115**, 064501.

- 64 F. P. Bretherton, The motion of long bubbles in tubes, *J. Fluid Mech.*, 1961, **10**, 166–188.
- 65 J. Blawzdziewicz, E. Wajnryb and M. Loewenberg, Hydrodynamic Interactions and Collision Efficiencies of Spherical Drops Covered with an Incompressible Surfactant Film, *J. Fluid Mech.*, 1999, **395**, 29–59.
- 66 S. Bhattacharya, J. Blawzdziewicz and E. Wajnryb, Hydrodynamic interactions of spherical particles in Poiseuille flow between two parallel walls, *Phys. Fluids*, 2006, **18**, 053301.

- 67 J. Blawzdziewicz, R. H. Goodman, N. Khurana, E. Wajnryb and Y.-N. Young, Nonlinear hydrodynamic phenomena in Stokes flow regime, *Physica D*, 2010, **239**, 1214.
- 68 K. B. Migler, String formation in sheared polymer blends: Coalescence, breakup, and finite size effects, *Phys. Rev. Lett.*, 2001, **86**, 1023–1026.
- 69 S. Kim and S. J. Karrila, *Microhydrodynamics: Principles* and *Selected Applications*, Butterworth-Heinemann, London, 1991.
- 70 P. Saffman and G. Taylor, The penetration of a fluid into a porous medium or Hele–Shaw cell containing a more viscous liquid, *Proc. R. Soc. A: Math. Phys. Eng.*, 1958, **245**, 312.